Potential Vorticity and the Quasigeostrophic and Semigeostrophic Mesoscale Vertical Velocity

ÁLVARO VIÚDEZ

Institut de Ciències del Mar, Barcelona, Spain

DAVID G. DRITSCHEL

Mathematical Institute, University of St Andrews, St Andrews, Fife, United Kingdom

(Manuscript received 28 January 2003, in final form 20 October 2003)

ABSTRACT

Results of a variety of numerical simulations are presented and the accuracy of quasigeostrophic (QG) and semigeostrophic (SG) vertical velocity estimates of the total vertical velocity is analyzed. The authors examine the dependence of the results on the potential vorticity (PV) anomaly of the flow, its time evolution, and the amount of numerical diffusion. The SG ω equation is solved in a novel way in the original physical coordinates rather than in geostrophic coordinates. A three-dimensional numerical model is used that *explicitly* conserves the PV on isopycnal surfaces through a contour-advective semi-Lagrangian (CASL) algorithm. The numerical simulations consist initially of one or two horizontal cylinders of anomalous PV: a shear zone that induces two or three counterflowing jets. These jets destabilize and break into cyclones or anticyclones. This is accompanied by enhanced vertical motion, which exhibits a dominantly balanced quadrupole pattern in horizontal cross sections, depending on the ellipticity of the gyres, together with weak second-order inertia–gravity waves. For flows containing only negative PV anomalies the magnitude of both the QG and SG vertical velocities are smaller than the magnitude of the total vertical velocity, while the opposite occurs for flows containing only positive PV anomalies. The reason for this behavior is that the QG ω equation misses a term proportional to the Laplacian of the horizontal velocity. A new, more accurate, ω equation is proposed to recover the vertical velocity when both experimental density and horizontal velocity data are available. The SG solution is nearly always more accurate than the QG solution, particularly for the largest vertical velocity values and when the flow has single-signed PV anomalies. For flows containing both positive and negative PV anomalies, for example, mushroomlike eddies, the QG vertical velocity is a better approximation to the total vertical velocity than the SG solution. The reason for this anomalous behavior lies in one additional assumption concerning the conservation of volume that is usually adopted to derive the SG ω equation.

1. Introduction

Oceanic mesoscale horizontal velocities are about 10^4 times as large as the cross-geopotential, vertical velocities. The mesoscale vertical velocity, though small in comparison with the horizontal velocity, is important, however, for the marine ecosystem since it is able to transport upward tens of meters of oceanic waters rich in nutrients from the dark deeper layers to the photic zone. But direct experimental measurements of mesoscale vertical velocities are difficult to carry out and, as a consequence, a number of indirect methods have been developed to estimate these vertical velocities. These methods were originally developed for atmospheric applications (Panofsky 1946, Sherman 1953). Among the most successful methods are those aimed at obtaining the quasigeostrophic (QG) vertical velocity (w^q) and the semigeostrophic (SG) vertical velocity (w^s) from the known density field ρ via the QG or SG ''omega'' equations (ω^q and ω^s equations, respectively). The original ω^q equation (see, e.g., Holton 1992, chapter 6.4) involved, however, an undesirable cancellation between terms (Trenberth 1978), which led Hoskins et al. (1978) to develop a new QG ''*Q*-vector'' ω^q equation. Generalizations of this ω^q equation beyond QG have since been developed by Davies-Jones (1991) and Viúdez et al. (1996a).

After Eliassen (1949) introduced the ''geostrophic momentum approximation'' and Yudin (1955) introduced ''geostrophic coordinates'' ($\hat{\mathbf{x}}$, $\hat{t}$), Hoskins and Draghici (1977) derived an equation for the SG vertical

Corresponding author address: Dr. Álvaro Viúdez, Institut de Ciències del Mar, P. Marítim 37, 08003-Barcelona, Spain.
E-mail: aviudez@cmima.csic.es

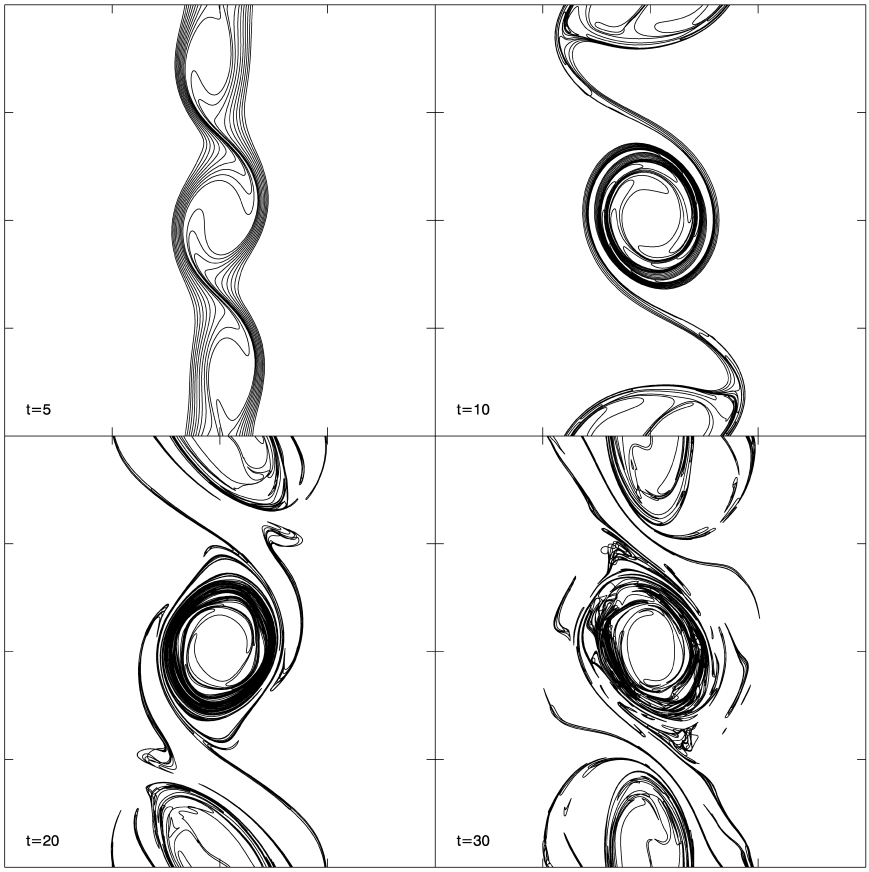

FIG. 1. Time evolution of the PV contours lying on the middle isopycnal surface $l = 32$ for the case of minimum PV anomaly $\varpi_0 = -0.75$ and $e_f = 10$. Times are indicated in inertial periods. There are 10 PV jumps in this layer, each with a magnitude of -0.075. The domain height is $L_z = 2\pi$ (which defines the unit of length) and the domain width is $L_x = L_y = cL_z$, where $c \equiv N/f = 100$.

velocity w^s that included the *ageostrophic* advection of the geostrophic horizontal velocity, which is neglected in QG theory. This ω^s equation was originally formulated and solved in the SG space $(\hat{\mathbf{x}}, \hat{t})$.

Both the QG and SG ω equations have been applied to the study of vertical velocity in oceanic mesoscale flows. Leach (1987) applied the ω^q equation, replacing space derivatives by inverse length scales, to estimate the order of magnitude of w in the ocean. A two-dimensional version of the QG ω equation was first solved for a density front in the Sargasso Sea (Pollard and Regier 1992). Fiekas et al. (1994) used the ω^q equation, in the approximate form used by Leach (1987), to obtain an order of magnitude estimate for w^q in a meandering jet, and Strass (1994) used the same approach with model data to compare the QG method with other diagnostic methods. Afterward, the full three-dimensional QG ω equation was solved to obtain the vertical circulation associated with the Atlantic front in the Alboran Sea (Viúdez et al. 1996b, 2000), the Azores front (Rudnick 1996), the Iceland–Færoes front (Allen and Smeed 1996), and the California Current (Shearman et al. 1999, 2000). The SG ω equation has less often been used to estimate oceanic circulations. A recent application to mesoscale subduction at the Antarctic polar front can be found in Naveira Garabato et al. (2001). Pinot et al. (1996) carried out a numerical study of the accuracy of the QG and SG vertical velocities in an oceanic frontal instability case and found that the QG solution overestimates the magnitude of the vertical velocity by about 10% while the SG solution was found to overestimate downwelling.

Here we present the results of a number of numerical simulations across a broad range of parameter space and examine how the accuracy of the QG and SG vertical velocities depends on (i) the Rossby number of the flow, (ii) the amount of numerical diffusion, and (iii) the time evolution of the flow. We also examine how the results depend on the prognostic variables used in the numerical model, a factor previously overlooked. To achieve this latter objective we use as a primary model a three-dimensional numerical model that explicitly conserves po-

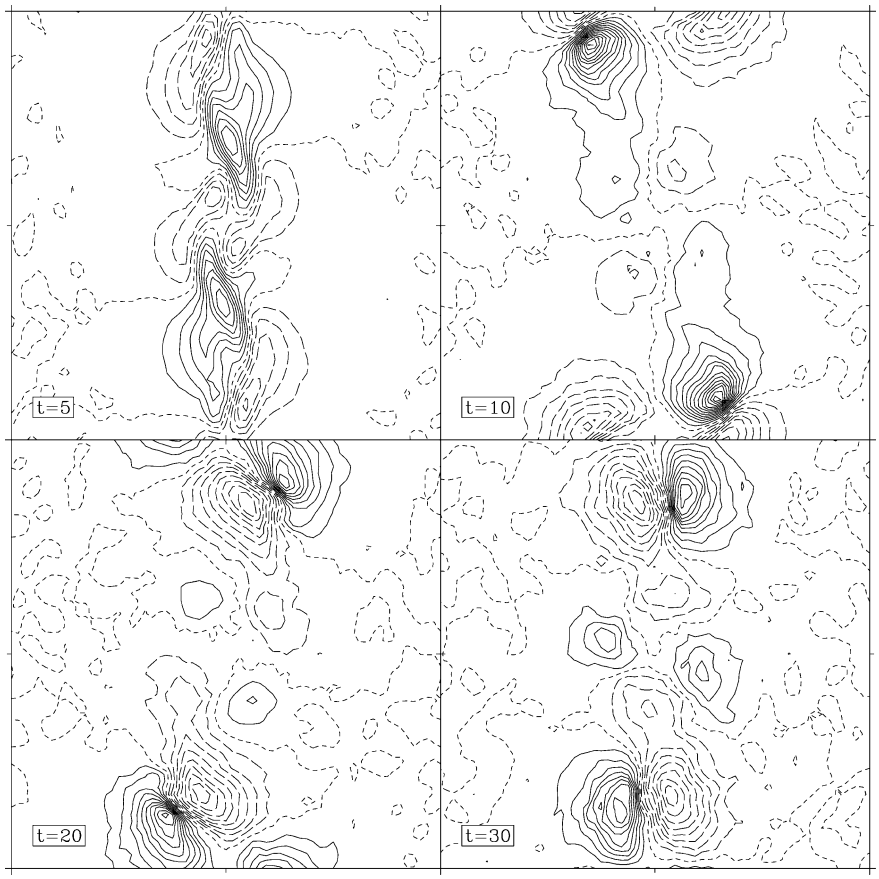

FIG. 2. Time evolution of the vertical velocity w in the horizontal layer $l_z = 28$ for the case $\varpi_0 = -0.75$ and $e_f = 10$. Times are indicated in inertial periods. Contour interval Δ is 2.5×10^{-5}.

tential vorticity (PV) on isopycnal surfaces through a contour-advective semi-Lagrangian algorithm (CASL; see Dritschel and Ambaum 1997) and, as a secondary model, one that does not make use of explicit PV conservation. The numerical simulations begin with one or two horizontal cylinders of anomalous PV that induce two or three counterflowing jets. The vertical velocity is analyzed over 30 inertial periods. During this period of time the jets destabilize and break into cyclones or anticyclones, depending on the sign of the PV anomaly, and vertical motion is enhanced.

The SG ω equation formulation is explained in section 2. This equation is here solved in the original space $(\mathbf{x}, t)$, thereby avoiding two additional field interpolations (and the implicit diffusion therewith). The numerical results are described in section 3. We find that, for flows containing only negative PV anomalies, the magnitude of both w^q and w^s is smaller than the magnitude of w, while just the opposite occurs for flows containing only positive PV anomalies. For flows containing PV anomalies of both signs, we find that the QG vertical velocity best approximates the total vertical velocity.

2. The SG and QG vertical velocity

The velocity field is denoted by $\mathbf{u} = \mathbf{u}_h + w\mathbf{k} = (u, v, w)$. Vector components here always refer to Cartesian components. Horizontal geostrophic velocity components are denoted $(u^g, v^g) = \mathbf{u}_h^g$. For any quantity χ we denote $\tilde{\chi} = \chi/f$, where f is the Coriolis parameter, taken to be constant.

a. The SG ω equation in geostrophic coordinates

Defining the SG space $(\hat{\mathbf{x}}, \hat{t})$:

$$\begin{aligned}\hat{\mathbf{x}}_h(\mathbf{x}, t) &\equiv \mathbf{x}_h - \boldsymbol{\nabla}_h \phi^g(\mathbf{x}, t)\\ &= (x, y) + [\tilde{v}^g(\mathbf{x}, t), -\tilde{u}^g(\mathbf{x}, t)],\\ \hat{z}(z) &\equiv z, \quad \text{and} \quad \hat{t}(t) \equiv t, \end{aligned} \tag{1}$$

where ϕ^g is the geopotential, and the SG ω equation may be written (Hoskins and Draghici 1977)

$$\hat{\nabla}_h^2(q^s \hat{w}) + \hat{w}_{\hat{z}\hat{z}} = 2\hat{\boldsymbol{\nabla}}_h \cdot \mathbf{Q}_h^s. \tag{2}$$

Subscripts $(x, y, z, \hat{x}, \hat{y}, \hat{z})$ denote partial derivatives. As

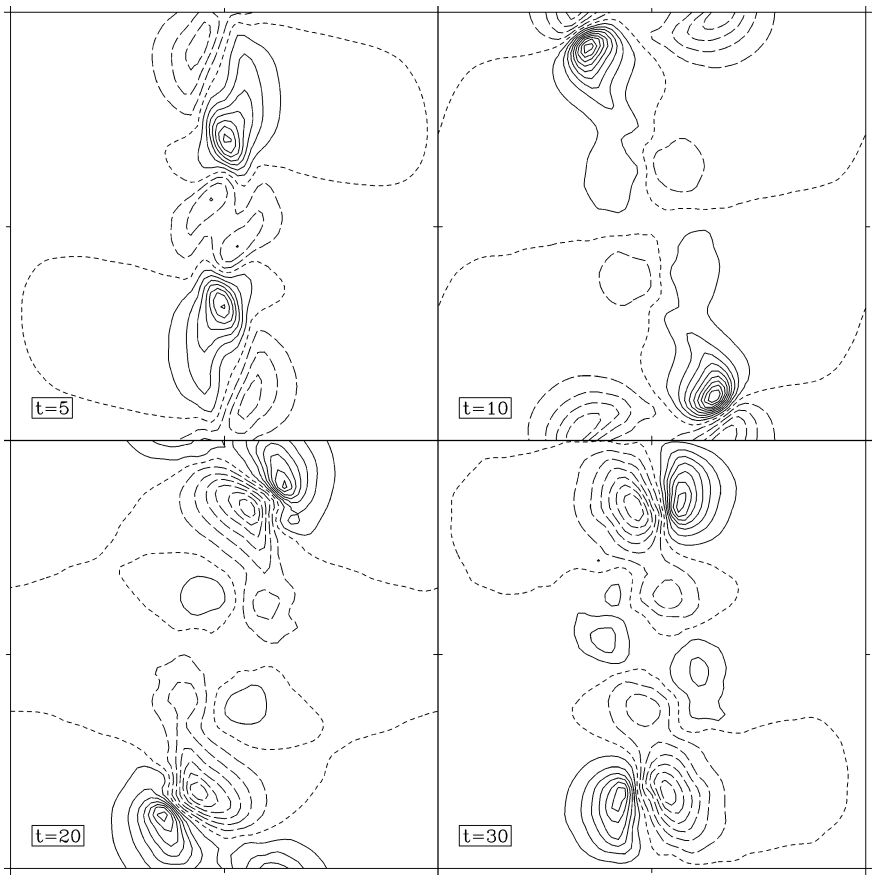

FIG. 3. As in Fig. 2 but for the QG vertical velocity w^q.

usual, for any function F with arguments (x, y, z, t), the symbols $F_{\hat{x}}$, $F_{\hat{y}}$, and $F_{\hat{z}}$ mean the $\hat{x}$, $\hat{y}$, and $\hat{z}$ partial derivative of the function G such that $G(\hat{x}, \hat{y}, \hat{z}, \hat{t}) = F(x, y, z, t,)$. We denote

$$\hat{\boldsymbol{\nabla}}_h F \equiv F_{\hat{x}}\mathbf{i} + F_{\hat{y}}\mathbf{j} \quad \text{and} \quad \hat{\boldsymbol{\nabla}}_h \cdot (F, G) \equiv F_{\hat{x}} + G_{\hat{y}}.$$

Note that the above expressions are coordinate dependent. A coordinate-independent version of the SG ω equation in direct vector notation is derived in section 2b.

The horizontal vector $\mathbf{Q}_h^s$ (the SG Q vector) and the scalar q^s (the SG PV) in (2) are geostrophic quantities defined by

$$\mathbf{Q}_h^s \equiv \hat{\boldsymbol{\nabla}}_h \mathbf{u}^g \cdot \hat{\boldsymbol{\nabla}}_h D \quad \text{and}$$
$$q^s \equiv N^2 \tilde{\boldsymbol{\zeta}}^s \cdot \boldsymbol{\nabla} d = c^2 \tilde{\zeta}^s - \tilde{\boldsymbol{\zeta}}^s \cdot \boldsymbol{\nabla} D.$$

Above,

$$\tilde{\boldsymbol{\zeta}}^s = (\tilde{\xi}^s, \tilde{\eta}^s, \tilde{\zeta}^s) = \tilde{\boldsymbol{\zeta}}^a + \mathbf{J}^g$$

is the sum of the dimensionless absolute geostrophic pseudovorticity

$$\tilde{\boldsymbol{\zeta}}^a \equiv (\boldsymbol{\nabla} \times \mathbf{u}_h^g + f\mathbf{k})/f = (-\tilde{v}_z^g, \tilde{u}_z^g, 1 + \tilde{v}_x^g - \tilde{u}_y^g),$$

and

$$\mathbf{J}^g \equiv \boldsymbol{\nabla}\tilde{u}^g \times \boldsymbol{\nabla}\tilde{v}^g$$
$$= (J_{yz}\{\tilde{u}^g, \tilde{v}^g\}, J_{zx}\{\tilde{u}^g, \tilde{v}^g\}, J_{xy}\{\tilde{u}^g, \tilde{v}^g\}),$$

where $J_{xy}\{F, G\} \equiv F_x G_y - F_y G_x$, and so on, is the Jacobian. In (2) the unknown field $\hat{w}$ is defined by

$$\hat{w} \equiv w^s/\tilde{\zeta}^s,$$

where w^s is the SG vertical velocity.

The isopycnal depth d and the scaled isopycnal displacement D used above are related to the density anomaly ρ' as follows: $\rho'(\mathbf{x}, t) \equiv \rho(\mathbf{x}, t) - \overline{\rho_z} z - \rho_0$, where ρ_0 and $\overline{\rho_z}$ are given constants. The value

$$d(\mathbf{x}, t) \equiv [\rho(\mathbf{x}, t) - \rho_0]/\overline{\rho_z}$$

is the *depth,* or vertical location, that the isopycnal located at $\mathbf{x}$ at time t has in the *reference density configuration* defined by $\overline{\rho_z} z + \rho_0$. The background squared Brunt–Väisälä frequency is $N^2 \equiv -g\overline{\rho_z}/\rho_0$, where g is the acceleration due to gravity, and $c \equiv N/f$ is the frequency ratio ($\epsilon \equiv f/N = c^{-1}$ is the inverse frequency

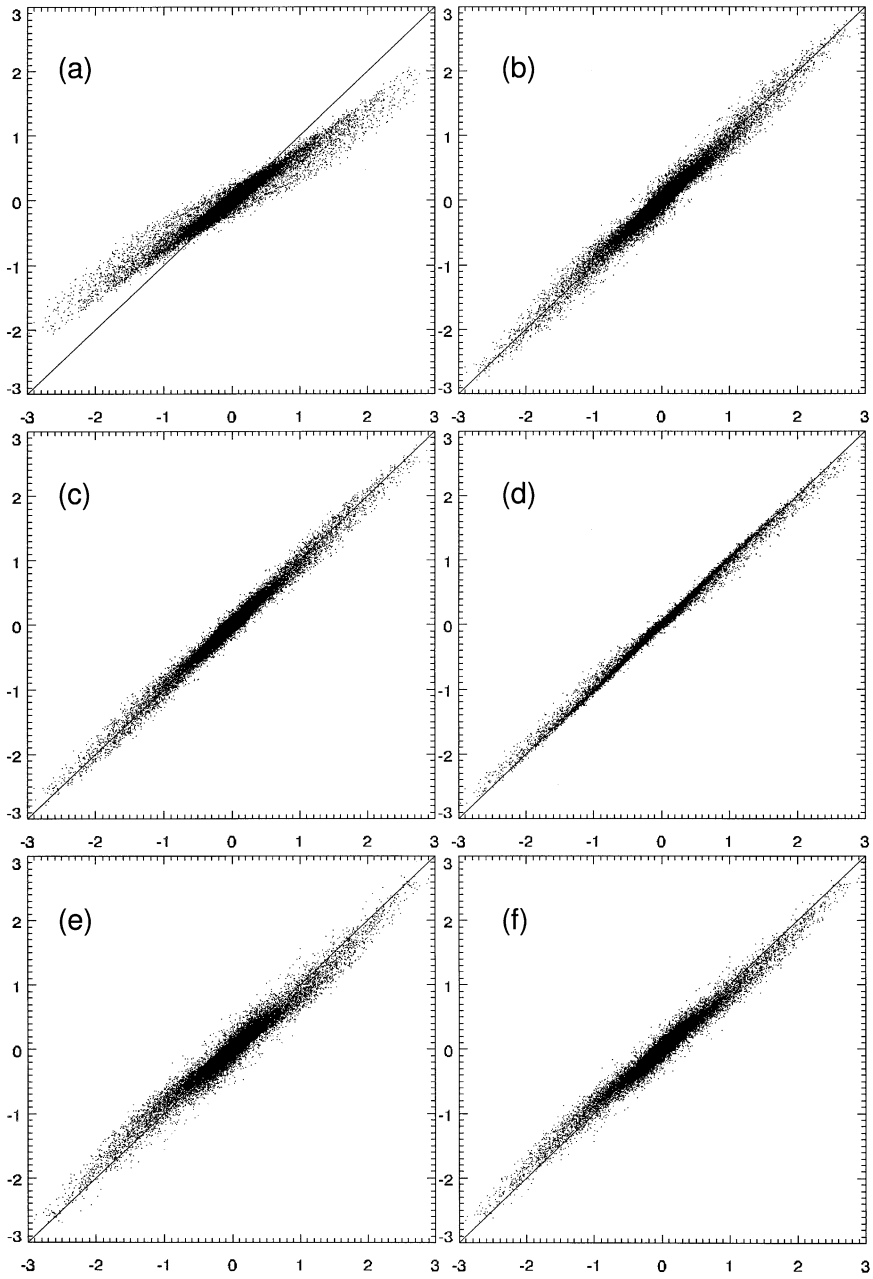

FIG. 4. Scatterplots of the total velocity w (horizontal axis, in units of 10^{-4}) for the case $\varpi_0 = -0.75$ and $e_f = 10$ vs (vertical axis) (a) the QG vertical velocity w^q, (b) the vertical velocity that results from including $\tilde{\zeta}_h' \cdot \nabla_h^2 \mathbf{u}_h^2$ on the right-hand side of the ω^q equation in (6), (c) the vertical velocity that results from including $\tilde{\zeta}_h' \cdot \nabla_h^2 \mathbf{u}_h^2 + 2\boldsymbol{\nabla}_h \cdot \mathbf{Q}_h'$ in (6), (d) the vertical velocity that results from including $\tilde{\zeta}_h' \cdot \nabla_h^2 \mathbf{u}_h^2 + 2\boldsymbol{\nabla}_h \cdot \mathbf{Q}_h' + \tilde{\zeta}_{zt}' + \mathbf{u}_h \cdot \boldsymbol{\nabla}_h \tilde{\zeta}_z'$ in (6), (e) the SG vertical velocity w^s, and (f) the SG vertical velocity that results from including the term $-\partial J'/\partial \hat{z}$ on the right-hand side of (4). Data for the entire domain are shown at $t = 20\ t_{\text{ip}}$.

ratio). The value $z - d(\mathbf{x}, t)$ is the *vertical displacement* of the isopycnal currently located at $(\mathbf{x}, t)$ with respect to its position in the reference configuration. Geostrophic quantities are conveniently defined using the *scaled isopycnal vertical displacement*

$$D(\mathbf{x}, t) \equiv c^2[z - d(\mathbf{x}, t)], \tag{3}$$

which is related to ρ by

$$f^2 D(\mathbf{x}, t) - N^2 z = g[\rho(\mathbf{x}, t)/\rho_0 - 1].$$

Thus, the geostrophic velocity shear can be defined

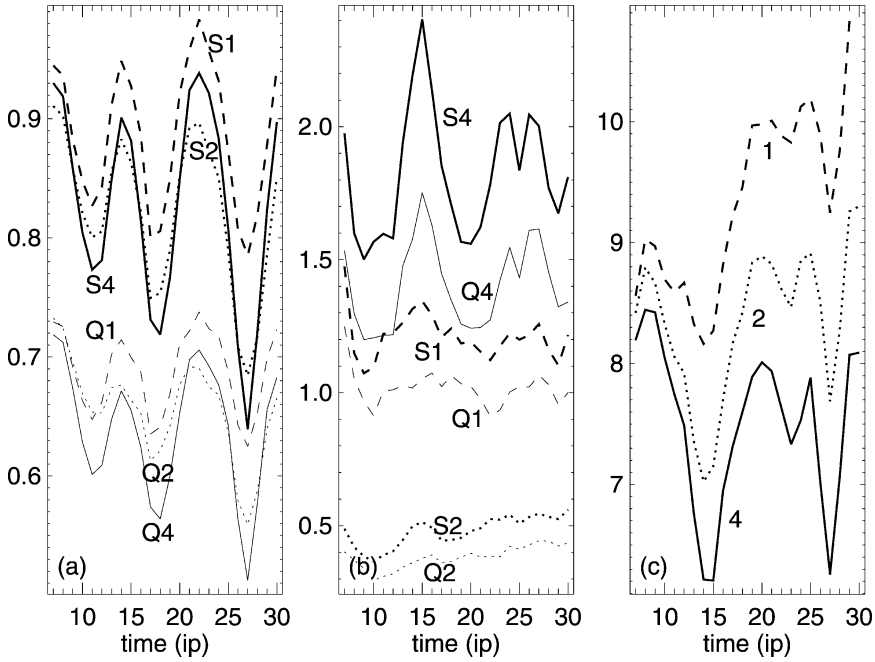

FIG. 5. (a) The slopes $s^q(t)$ and $s^s(t)$ and (b) the probable uncertainties $\sigma^q(t)$ and $\sigma^s(t)$ (in units of 10^{-4}) in the estimate of s in the linear regressions $w^q(\mathbf{x}, t) = \beta^q(t) + s^q(t)w(\mathbf{x}, t)$ (symbol Q) and $w^s(\mathbf{x}, t) = \beta^s(t) + s^s(t)w(\mathbf{x}, t)$ (symbol S), as a function of time and for the different values of $e_f = 1$ (labeled with 1), 10 (labeled with 2), and 1000 (labeled with 4). The linear fit is computed once every inertial period, using magnitudes of w, w^q, and w^s larger than 0.5×10^{-5}. (c) The spatial average of the absolute total velocity $\langle |w| \rangle(t)$ (in units of 10^{-6}).

through the "thermal wind" expression as $\tilde{\mathbf{u}}_z^g \equiv -\mathbf{k} \times \nabla_h D = (D_y, -D_x)$, and the horizontal gradient of D may be interpreted as the dimensionless horizontal geostrophic pseudovorticity $\tilde{\boldsymbol{\zeta}}_h^g = (-\tilde{v}_z^g, \tilde{u}_z^g) = \nabla_h D$.

b. The SG ω equation in original coordinates

We follow here a new approach and solve the SG ω equation [(2)] in the original coordinates $(\mathbf{x}, t)$. This method requires solving an equation more complicated than (2) in the SG space, but it avoids a first interpolation of the known coefficients to the space $(\hat{\mathbf{x}}, \hat{t})$, as well as a second interpolation of the solution back to the space $(\mathbf{x}, t)$ for purposes of comparison with the total and QG vertical velocity.

Using the chain rule,

$$\nabla F = \frac{\partial F}{\partial \hat{\mathbf{x}}} \frac{\partial \hat{\mathbf{x}}}{\partial \mathbf{x}} = \mathsf{R} \cdot \hat{\nabla} F,$$

where, in dyadic notation, $\mathsf{R} = \partial \hat{\mathbf{x}}/\partial \mathbf{x} = \partial \hat{x}_i/\partial x_j \mathbf{e}_j \mathbf{e}_i$. The Cartesian components of the tensor $\mathsf{R} = \nabla \hat{\mathbf{x}} = \mathbf{1} - \nabla \nabla_h \phi^g$ and its inverse L are

$$\mathsf{R} = \mathbf{1} + \begin{bmatrix} \tilde{v}_x^g & -\tilde{u}_x^g & 0 \\ \tilde{v}_y^g & -\tilde{u}_y^g & 0 \\ \tilde{v}_z^g & -\tilde{u}_z^g & 0 \end{bmatrix} \quad \text{and}$$

$$\mathsf{L} = \mathsf{R}^{-1} = \frac{1}{\tilde{\zeta}^s} \begin{bmatrix} 1 - \tilde{u}_y^g & \tilde{u}_x^g & 0 \\ \tilde{u}_x^g & 1 + \tilde{v}_x^g & 0 \\ \tilde{\xi}^s & \tilde{\eta}^s & \tilde{\zeta}^s \end{bmatrix}.$$

Thus, the gradient, horizontal divergence, and vertical derivative in the space $(\hat{\mathbf{x}}, \hat{t})$ are related to the derivatives in the space $(\mathbf{x}, t)$ by

$$\hat{\nabla} F = \mathsf{L} \cdot \nabla F, \qquad \hat{\nabla}_h \cdot \mathbf{F}_h = \mathsf{L}_h^{\mathrm{T}} : \nabla_h \mathbf{F}_h, \quad \text{and}$$

$$\frac{\partial F}{\partial \hat{z}} = \frac{\boldsymbol{\zeta}^s}{\zeta^s} \cdot \nabla F,$$

where $\mathsf{A} : \mathsf{B} \equiv \Sigma_{ij} A_{ij} B_{ij}$ is the scalar product of tensors A and B. Using these relations, the SG ω equation [(2)] is expressed in the space $(\mathbf{x}, t)$ as

$$\mathsf{L}_h^{\mathrm{T}} : \nabla_h [\mathsf{L}_h \cdot \nabla_h (q^s \hat{w})] + \frac{\boldsymbol{\zeta}^s}{\zeta^s} \cdot \nabla \left(\frac{\boldsymbol{\zeta}^s}{\zeta^s} \cdot \nabla \hat{w} \right) = 2 \mathsf{L}_h^{\mathrm{T}} : \nabla_h \mathbf{Q}_h^s, \tag{4}$$

where

$$\mathbf{Q}_h^s = (\mathsf{L}_h \cdot \nabla_h \mathbf{u}_h^g) \cdot (\mathsf{L}_h \cdot \nabla_h D). \tag{5}$$

In the limit $\tilde{\zeta}^s \to 1$, $\mathsf{L} \to \mathbf{1}$, and $q^s \to c^2$, (4) and (5) yield the QG ω equation

$$c^2 \nabla_h^2 w^q + w_{zz}^q = 2 \nabla_h \cdot \mathbf{Q}_h^g, \tag{6}$$

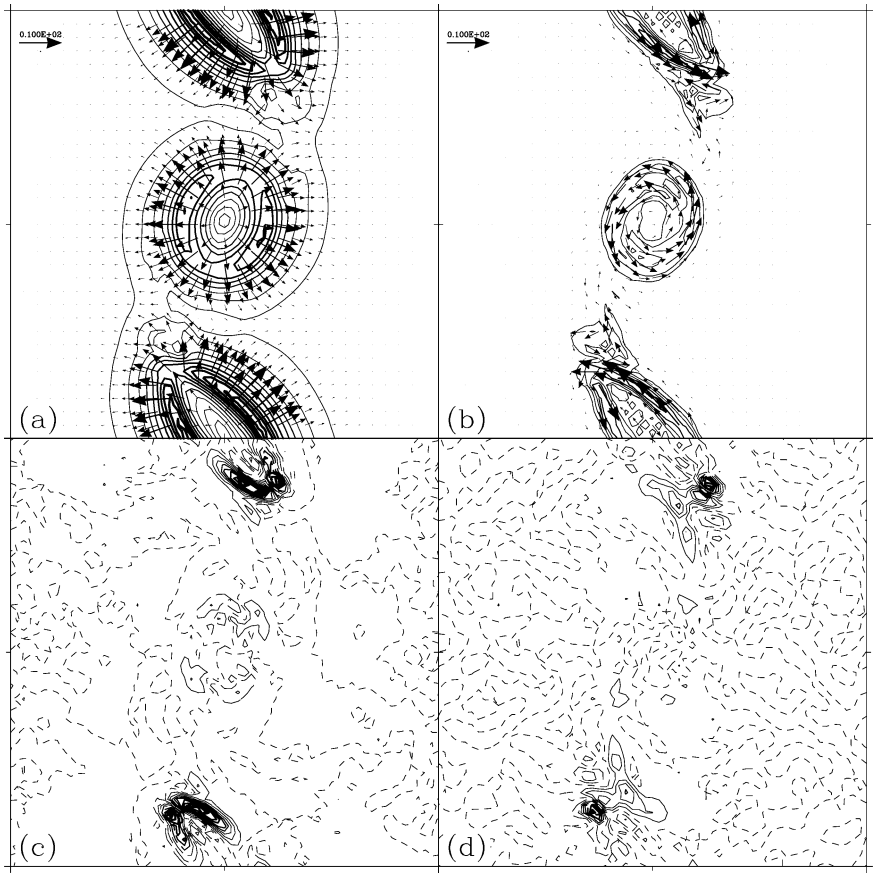

FIG. 6. (a) Ageostrophic horizontal pseudovorticity $\tilde{\zeta}'_h$ ($\Delta = 2.5$, contours indicate the magnitude, reference vector is 25), (b) horizontal Laplacian of the horizontal velocity $\nabla_h^2\mathbf{u}_h$ ($\Delta = 2 \times 10^{-4}$, reference vector is 10^{-3}), (c) $\tilde{\zeta}'_h \cdot \nabla_h^2\mathbf{u}_h$ ($\Delta = 5 \times 10^{-4}$), and (d) $2\nabla_h \cdot \mathbf{Q}^g$ ($\Delta = 2 \times 10^{-3}$). The fields shown lie in the horizontal layer $l_z = 28$ at $t = 20t_{\text{ip}}$.

where

$$\mathbf{Q}_h^g \equiv \boldsymbol{\nabla}_h\mathbf{u}_h^g \cdot \boldsymbol{\nabla}_h D$$

is the QG Q vector and w^q is the QG vertical velocity.

The SG ω equation [(4)] is solved by relaxation, using as a first guess $w^q/\tilde{\zeta}^s$, where w^q is obtained by direct inversion of the QG ω equation [(6)] in spectral space. Convergence of the iterative method is reached when the ratio $r\{\hat{w}^n\}/T$ of the domain average residual of the nth solution $\hat{w}^n$,

$$r\{\hat{w}^n\} \equiv \left\langle \left| \underbrace{\mathsf{L}_h^{\mathrm{T}} : \boldsymbol{\nabla}_n[\mathsf{L}_h \cdot \boldsymbol{\nabla}_h(q^s\hat{w}^n)]}_{T_1} + \underbrace{\frac{\boldsymbol{\zeta}^s}{\zeta^s} \cdot \boldsymbol{\nabla}\left(\frac{\boldsymbol{\zeta}^s}{\zeta^s} \cdot \boldsymbol{\nabla}\hat{w}^n\right)}_{T_2} - \underbrace{2\mathsf{L}_h^{\mathrm{T}} : \boldsymbol{\nabla}_h\mathbf{Q}_h^s}_{T_3} \right| \right\rangle,$$

to $T \equiv \max\{\langle|T_1|\rangle, \langle|T_2|\rangle, \langle|T_3|\rangle\}$ is smaller than a tolerance value ϵ_0, here taken to be 5×10^{-3}. In practice, this implies pointwise convergence of w^s to within $10^{-5}\max|w^s|$.

Last, for further reference, we write down the generalized ω equation (Viúdez et al. 1996a),

$$\frac{d\tilde{\zeta}'_z}{dt} = -\boldsymbol{\nabla}_h \cdot [2\mathbf{Q}_h + (D_z - c^2)\boldsymbol{\nabla}_h w] + (\tilde{\zeta} + 1)w_{zz} + \tilde{\boldsymbol{\zeta}}'_{hz} \cdot \boldsymbol{\nabla}_h w - \tilde{\boldsymbol{\zeta}}'_h \cdot \nabla_h^2\mathbf{u}_h, \quad (7)$$

where $\boldsymbol{\zeta}'_h \equiv (-v + v^g, u - u^g)_z$ is the ageostrophic horizontal pseudovorticity, $\zeta' \equiv \zeta - \zeta^g = (v - v^g)_x -$

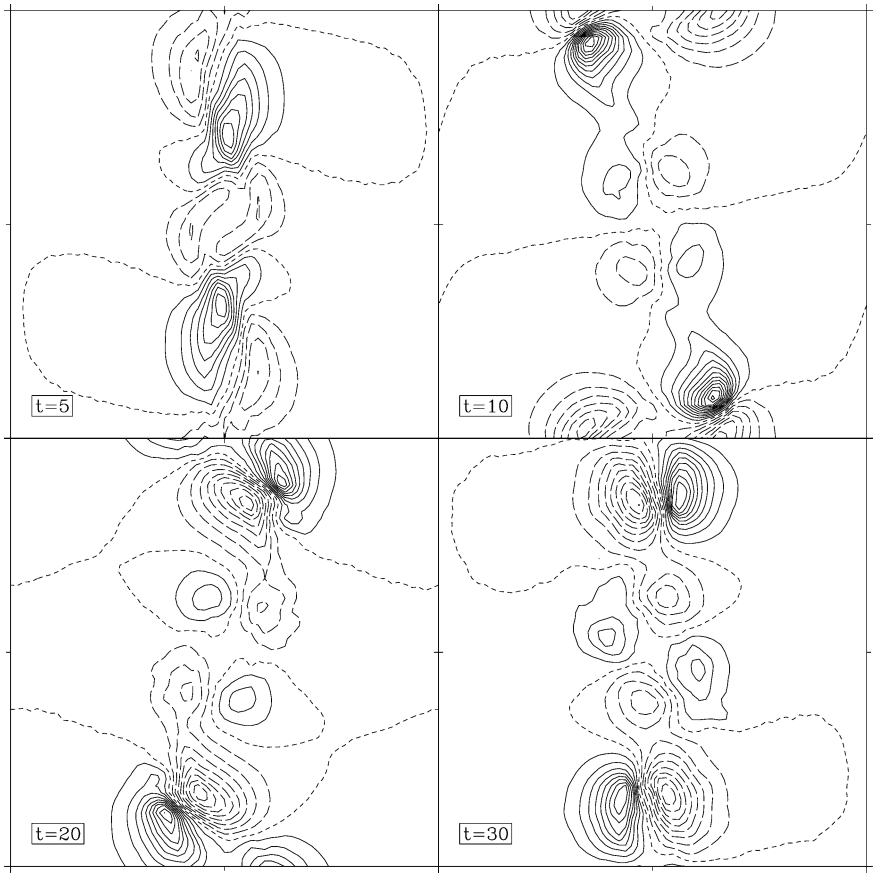

FIG. 7. As in Fig. 2 but for the SG vertical velocity w^s.

$(u - u^g)_y$ is the ageostrophic vertical vorticity, and $\mathbf{Q}_h \equiv \nabla_h \mathbf{u}_h \cdot \boldsymbol{\nabla}_h D$ is a generalized Q vector. Under the QG approximation, the horizontal velocity is replaced by its geostrophic approximation ($\mathbf{u}_h \to \mathbf{u}_h^g$) and, assuming that for small Rossby numbers the flow is both inertially strongly stable ($|\tilde{\zeta}| \ll 1$) and statically strongly stable ($|D_z| \ll c^2$), the Q vector ω equation [(7)] reduces to the QG Q vector ω equation [(6)].

3. Numerical results

a. The numerical model

The primary numerical model is a three-dimensional, triply periodic, pseudospectral model of an incompressible, rotating, stratified fluid under the Oberbeck–Boussinesq approximation [see Dritschel and Viúdez (2003) for details]. There are three prognostic equations, two for the horizontal components of ageostrophic vorticity and a third one for PV. Conservation of PV is made explicit through the CASL algorithm (Dritschel and Ambaum 1997) on isopycnal surfaces. Both the nondivergent velocity $\mathbf{u}$ and the isopycnal vertical displacement D fields are defined from a three-dimensional vector potential. The horizontal components of this vector potential are directly obtained from the horizontal ageostrophic vorticity, while the vertical component is obtained from the inversion of the definition of PV. This approach, hereinafter referred to as the $\mathcal{AB}\varpi$ model, is explained in more detail in appendix A.

The numerical parameters used in all of the simulations described below are identical. We use a 64^3 grid together with 64 isopycnal surfaces, a frequency ratio $c \equiv N/f = 100$, a domain height $L_Z = 2\pi$ (which defines the unit of length), a domain width $L_X = L_Y = cL_Z$, mean buoyancy frequency $N = 2\pi$ (which defines the unit of time), and a time step $\delta t = 0.1$. One *buoyancy period* is therefore the unit of time $t_{\rm bp} \equiv 2\pi/N = 1$, while one inertial period $t_{\rm ip} = 100\ t_{\rm bp}$ since $t_{\rm ip} \equiv 2\pi/f$.

A biharmonic hyperdiffusion term $-\mu(\nabla^4\mathcal{A}, \nabla^4\mathcal{B})$ is added to the equations for the rate of change of the horizontal ageostrophic vorticity ($\mathcal{A}$, $\mathcal{B}$). The hyperviscosity coefficient μ is chosen by specifying the damping rate (e folding, e_f) of the largest wavenumber in spectral space *per inertial period*. Here we present results using several damping rates ranging from very low diffusion ($e_f = 1$), to low diffusion ($e_f = 10$), to large diffusion ($e_f = 1000$). Note that $t_{\rm ip} = ct_{\rm bp}$, and $c = N/f \gg 1$. That is, with $e_f = 1$ the damping rate per buoyancy period is extremely small.

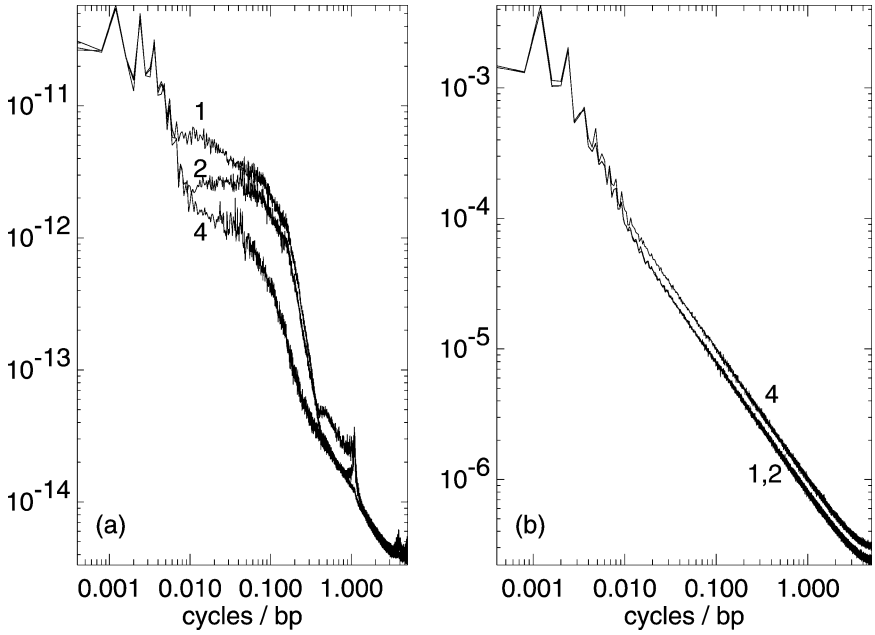

FIG. 8. Averaged frequency spectra for (a) w^2 and (b) 2 times the specific kinetic energy ($u^2 + v^2 + w^2$) for the case $\varpi_0 = -0.75$ with $e_f = 1$ (labeled 1), 10 (labeled 2), and 1000 (labeled 4). The horizontal axis is frequency in cycles per buoyancy period. Every spectra is the average of 8^3 spectra, each computed from the time series from $t = 500$ ($5t_{ip}$) to $t = 3000$ ($30\ t_{ip}$) with a time interval of 0.1 (thus comprising $25\,000 \times 8^3$ data points).

Last, we use an initialization procedure based on the progressive growth of the PV field during the first five inertial periods. This procedure largely suppresses the generation of inertia–gravity waves, leading to a nearly balanced flow. Further details of the theoretical and numerical approach and the initialization technique are explained in Viúdez and Dritschel (2003) and Dritschel and Viúdez (2003).

b. Cylindrical shear zone

A shear zone is simulated by a horizontal cylinder [of circular cross section in the vertically stretched space (x, y, cz)] of anomalous PV. This distribution of PV induces two counterflowing jets at the horizontal extremities of the cylinder. The horizontal and vertical radius of the cylinder are $0.5c$ and 0.5, respectively. The cylinder has 10 PV levels in the middle isopycnal surface ($l = 32$). We compare the total, QG, and SG vertical velocities for different cases ranging from a highly ageostrophic anticyclonic flow with a minimum PV anomaly of $\varpi_0 = -0.75$, to a highly ageostrophic cyclonic flow with a maximum PV anomaly of $\varpi_0 = 1.50$. We also vary the diffusion coefficient in selected cases.

1) FLOWS WITH ONLY NEGATIVE PV ANOMALIES

The PV contours for the case $\varpi_0 = -0.75$ and $e_f = 10$ are shown in Fig. 1 from the end of the initialization period ($t = 5t_{ip}$) to the end of the simulation ($t = 30\ t_{ip}$). In this case the time average of the (minimum) Rossby number is -0.60 and the time average of the maximum Froude number is 0.35. The Froude number is defined here as the ratio $\omega_h/\mathcal{N}$ between the magnitude of the horizontal vorticity $\omega_h \equiv |\boldsymbol{\omega}_h|$ to the total Brunt–Väisälä frequency $\mathcal{N} \equiv (-g\rho_z/\rho_0)^{1/2} = N(1 - \epsilon^2 D_z)^{1/2}$. In this simulation the PV rolls up into a street of anticyclonic vortices that remain separated. The w field (Fig. 2) exhibits a quadrupolar pattern in each horizontal cross section. This pattern is associated with the ellipsoidal shape of the developing vortices, with upward (downward) motion upstream (downstream) of the ridges in every vortex [see Viúdez and Dritschel (2003) for a physical interpretation]. Small, second-order inertia–gravity waves are also clearly visible. The maximum vertical velocities are about 3.0×10^{-4}. The gyre that forms in the center of the domain has smaller vertical velocities due to its smaller ellipticity. This quadrupolar vertical velocity pattern moves anticyclonically along with the rotating gyres and persists throughout the simulation.

The QG vertical velocity w^q (Fig. 3) reproduces the quadrupole pattern of w but its magnitude is somewhat smaller. Maximum absolute values of w^q are about 2.0×10^{-4}. The w^q field does not reproduce the fine structure visible in the w field and, as expected, w^q is virtually free of inertia–gravity wave motion. A scatterplot of w^q versus w at time $t = 20\ t_{ip}$ (Fig. 4a) clearly shows that $|w^q|$ is smaller than $|w|$. The time evolution of the slope $s^q(t)$ in the linear regression

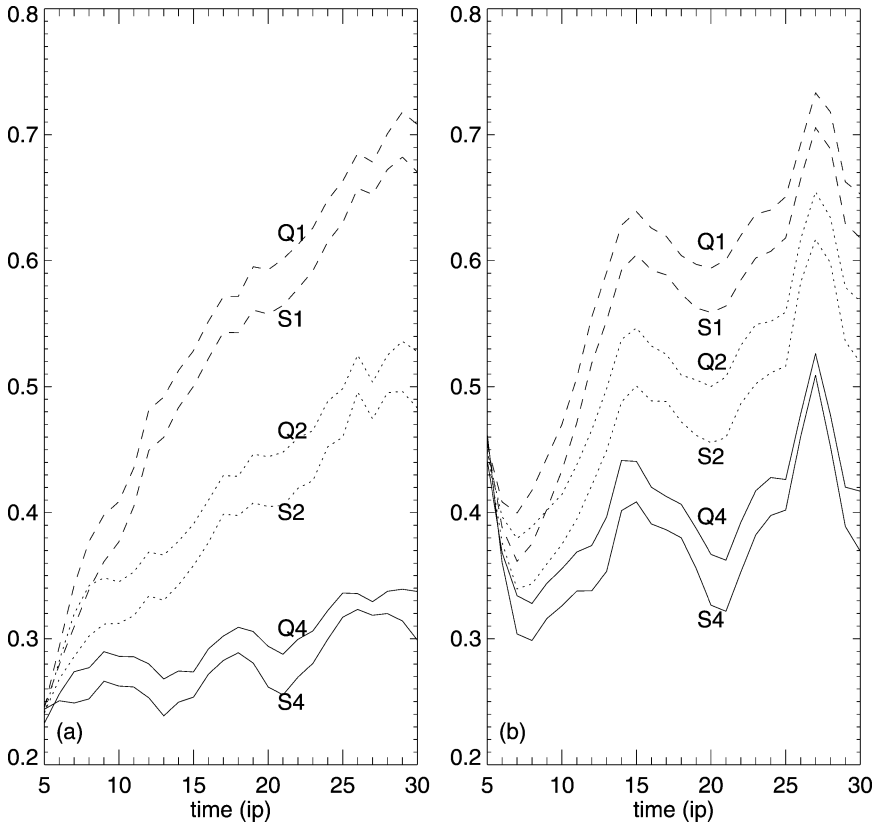

FIG. 9. (a) The average difference $\langle |w - w^q| \rangle \times 10^5$ (symbol Q) and $\langle |w - w^s| \rangle \times 10^5$ (symbol S) as a function of time and for the different values of $e_f = 1$ (symbol 1), 10 (symbol 2), and 1000 (symbol 4). (b) Same as (a) but for the normalized average difference $\langle |w - w^q| \rangle / \langle |w| \rangle$ (symbol Q) and $\langle |w - w^s| \rangle / \langle |w| \rangle$ (symbol S).

$$w^q(\mathbf{x}, t) = \beta^q(t) + s^q(t)w(\mathbf{x}, t),$$

(Fig. 5a) shows that $s^q(t)$ ranges mostly between 0.6 and 0.7, but exceptionally low values of $s^q(t)$ close to 0.5 occur at $t = 27t_{ip}$ near the minimum of the average vertical velocity $\langle |w| \rangle$ (Fig. 5c). The slope $s^q(t)$ is closer to 1 for very low diffusion ($e_f = 1$) than for low and high diffusion ($e_f = 10$ and $e_f = 1000$). Thus, diffusion worsens the comparison between the actual and diagnosed vertical velocity fields.

The main reason why w^q is smaller than w in flows with negative PV appears to be the omission of the term $\tilde{\boldsymbol{\zeta}}'_h \cdot \nabla_h^2 \mathbf{u}_h$ in the QG ω equation in (6). This term is present, however, in the generalized ω equation in (7). Adding this term to the right-hand side of (6) results in a significant increase in the slope in the scatterplot (Fig. 4b). The analysis of $\tilde{\boldsymbol{\zeta}}'_h \cdot \nabla_h^2 \mathbf{u}_h$ is shown in Fig. 6. The ageostrophic horizontal pseudovorticity $\tilde{\boldsymbol{\zeta}}'_h$ (Fig. 6a) is always directed out of the cyclonic vortices, implying that the ageostrophic shear velocity $\mathbf{u}'_{hz}$ is mainly in the same direction as $\mathbf{u}_h$; that is, the vortices are supergeostrophic. The Laplacian $\nabla_h^2 \mathbf{u}_h$ (Fig. 6b) is mainly opposite to $\mathbf{u}_h$. The product of both terms $\tilde{\boldsymbol{\zeta}}'_h \cdot \nabla_h^2 \mathbf{u}_h$ (Fig. 6c) is, however, positive (negative) upstream (downstream) of the troughs, that is, of the same sign as the horizontal divergence of $\mathbf{Q}_h^g$ (Fig. 6d), whose magnitude is larger than $|\tilde{\boldsymbol{\zeta}}'_h \cdot \nabla_h^2 \mathbf{u}_h|$. Thus, $\tilde{\boldsymbol{\zeta}}'_h \cdot \nabla_h^2 \mathbf{u}_h$ is a term that increases the magnitude of the vertical velocity in the generalized ω equation. It is expected therefore that the omission of this term (as done in the QG ω equation) will result in an underestimation of the vertical velocity in flows with negative PV.

The second most important term in (7), missing in (6), is the ageostrophic part in the divergence of $\mathbf{Q}_h$, that is, $2\boldsymbol{\nabla}_h \cdot \mathbf{Q}'_h$, where $\mathbf{Q}'_h \equiv \mathbf{Q}_h - \mathbf{Q}_h^g$. Including this term in (6) results also in an improvement in the slope (Fig. 4c) but it is not so important as including $\tilde{\boldsymbol{\zeta}}'_h \cdot \nabla_h^2 \mathbf{u}_h$. Taking into account the material rate of change of the ageostrophic differential vertical vorticity, $\tilde{\zeta}'_{zt} + \mathbf{u}_h \cdot \boldsymbol{\nabla}_h \tilde{\zeta}'_z$ (Fig. 4d) seems to reduce the scatter; that is, interestingly it accounts mainly for the vertical velocity associated with wave motion.

The SG vertical velocity w^s (Fig. 7) reproduces the quadrupole pattern of w as well. The magnitude of w^s is significantly larger than $|w^q|$ but still smaller than $|w|$. Maximum $|w^s|$ values are about 2.5×10^{-4}. The SG solution is, like w^q, virtually free of inertia–gravity

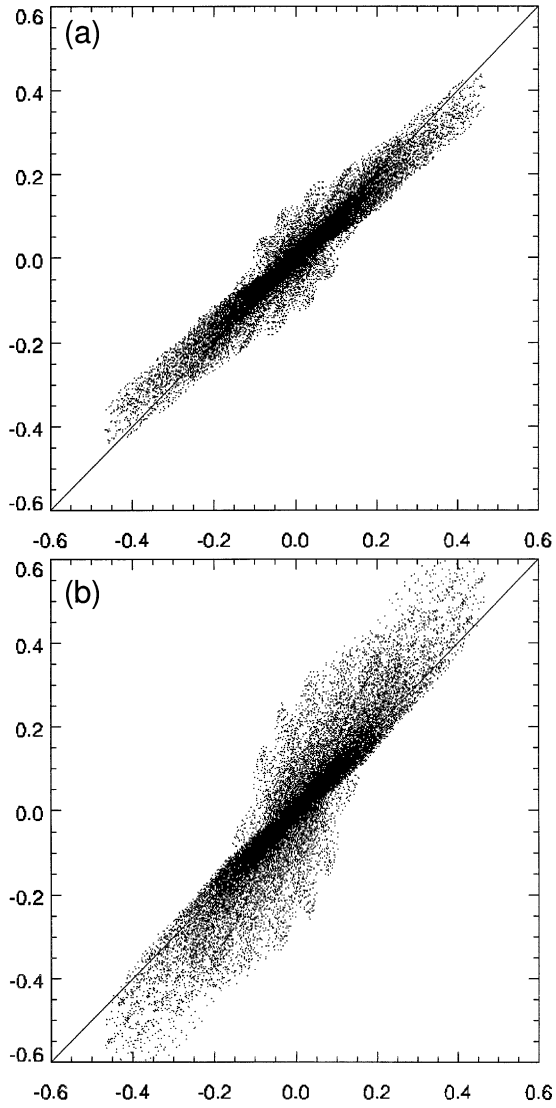

FIG. 10. Scatterplots (as in Figs. 4a,e) of (a) w^q and (b) w^s for the case $\varpi_0 = -0.75$ and $e_f = 300$ using the results of the $\mathcal{ABC}$ model (in units of 10^{-5}) at $t = 20\ t_{ip}$.

wave motion. The scatterplot of w^s versus w at $t = 20\,t_{ip}$ (Fig. 4e) shows that the slope of w^s gets closer to 1 than does the slope of w^q (Fig. 4a), but it is still smaller than 1. Quantitatively, the slope $s^s(t)$ in the linear regression

$$w^s(\mathbf{x}, t) = \beta^s(t) + s^s(t)w(\mathbf{x}, t),$$

(Fig. 5a) is always closer to 1 that $s^q(t)$, and ranges mostly between 0.7 and 0.95. An exception again occurs around the minimum of $\langle|\omega|\rangle$ (Fig. 5b). Both slopes s^q and s^s show coherent oscillations, which do not seem to have a clear relation with the average vertical velocity except at $t = 27\ t_{ip}$. Again, $s^s(t)$ is smaller for very low diffusion ($e_f = 1$) than for low and high diffusion ($e_f = 10$ and $e_f = 1000$), but the slopes of the latter two are again similar.

The w^s scatter, however, does not seem to be smaller than that of w^q. As expected from a visual inspection of the scatterplots (Fig. 4e), the probable uncertainty $\sigma^s(t)$ in the estimate of s^s is larger than $\sigma^q(t)$ for all the diffusion coefficients. Thus, the scatter of the SG solution w^s is larger than the scatter of the QG solution w^q. The scatter for $e_f = 10$ is larger than for $e_f = 1$, but smaller than for $e_f = 1000$. This fact might be related to the presence of the inertia–gravity waves as explained next.

The average spectra of the squared vertical velocity w^2 (Fig. 8a) shows the presence of inertia–gravity waves with frequencies between f and N (cycles per buoyancy period between 0.01 and 1). The vertical motion is however close to a balanced state because the vertical velocity components with frequencies smaller than f still dominate the spectra. Diffusion reduces significantly the inertia–gravity wave vertical motion but leaves the slow motion approximately unchanged. The inertia–gravity wave motion is relatively small, appreciable in the vertical velocity but negligible in the horizontal motion, as shown in the kinetic energy spectra (Fig. 8b). The damping of inertia–gravity waves for the case $e_f = 10$ relative to $e_f = 1$ may also be seen in the reduced scatter shown in Fig. 5b. For very large diffusion ($e_f = 1000$) the vertical inertia–gravity wave motion is damped as well, but the spectral components of kinetic energy experience a significant *increase* at all frequencies smaller than the inertial one (Fig. 8b). Thus, very high diffusion may induce, through an increase of horizontal motion, non-QG and non-SG vertical velocities, which may explain the larger values of the scatter, since neither the QG nor the SG solutions take into account diffusion of momentum.

The average difference $\langle|w - w^q|\rangle$ (Fig. 9a) is always larger than $\langle|w - w^s|\rangle$ irrespective of the diffusion. These averaged quantities increase in time during the first 35 inertial periods, after which an almost steady state is reached (not shown). It is observed that the smaller the diffusion the larger the rate of change of the average differences $\langle|w - w^q|\rangle$ and $\langle|w - w^s|\rangle$. This fact might be related to the generation of vertical motion due to inertia–gravity waves because the difference $\langle|w - w^s|\rangle - \langle|w - w^q|\rangle$ remains almost constant with time, and the ratios $\langle|w - w^q|\rangle/\langle|w|\rangle$ and $\langle|w - w^s|\rangle/\langle|w|\rangle$ (Fig. 9b) do not exhibit this monotonous increase. Most important, Fig. 9a shows that the differences between the average vertical velocity values in simulations with different diffusion coefficients and identical dynamics, QG or SG, are larger than the differences between the values with different dynamics but identical diffusion coefficients. Thus, the amount of diffusion seems to be more important in the absolute comparison of vertical velocities than the choice of the QG or SG approximation.

Numerical integrations carried out with the $\mathcal{ABC}$ mod-

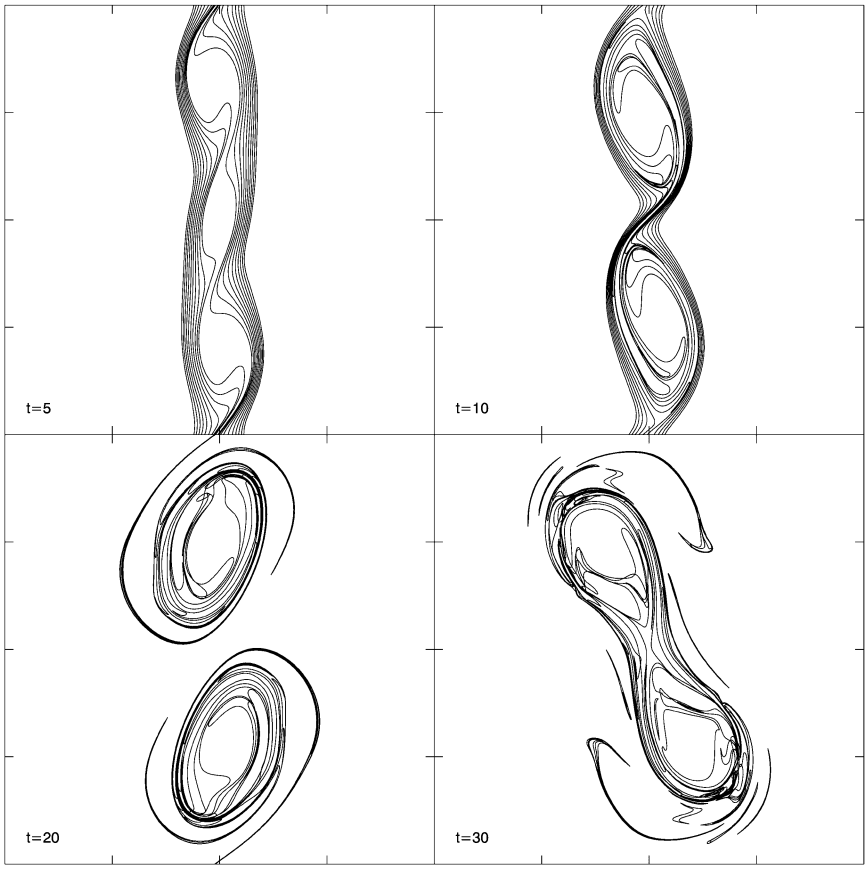

FIG. 11. PV contours (as in Fig. 1) for the case of maximum PV anomaly $\varpi_0 = 1.25$.

el, which follows the same approach as the $\mathcal{AB}\varpi$ model except that PV is not explicitly conserved (see appendix A), required a larger value of the numerical diffusion for stability. For the case $\varpi_0 = -0.75$ a value of $e_f > 200$ was required to control the growth of grid-scale numerical noise during the time integration. This large diffusion has important consequences for the vertical motion, as can be observed in the scatterplots in Fig. 10. In this case, as a result of the reduced PV gradients, the vertical velocities are about five times smaller, and the scatter is larger, than those given by the $\mathcal{AB}\varpi$ model (Fig. 4). Diffusion of PV is thus seen to have a serious impact on the computation of vertical velocities.

2) FLOWS WITH ONLY POSITIVE PV ANOMALIES

In the next simulation for a *cyclonic* PV anomaly (with $\varpi_0 = 1.25$ and $e_f = 10$, Fig. 11) the PV contours roll up into a street of cyclonic vortices that merge at about $t = 28\ t_{ip}$. In this case the ellipticity of the cyclonic vortices is similar so that the horizontal distribution of w exhibits a similar quadrupole pattern in every gyre (Fig. 12) with downward (upward) motion upstream (downstream) of the troughs. Small, second order inertia–gravity waves are again also visible. The maximum absolute vertical velocities are about 0.90×10^{-4}, more than 3 times as small as in the anticyclonic case with $\varpi_0 = -0.75$ shown in Fig. 1. Once the vortices merge, the vertical velocity field near the end of the simulation ($t = 30\ t_{ip}$) becomes a single quadrupole pattern associated with one large ellipsoidal vortex. In this case the time average of the (maximum) Rossby number is 0.44 and the time average of the maximum Froude number is 0.22.

The QG vertical velocity w^q (Fig. 13) reproduces the quadrupole pattern of w but with a magnitude in this case *larger* than $|w|$, having maximum absolute values around 1.0×10^{-4}, as is also observed in the scatterplot of w^q versus w at time $t = 20\ t_{ip}$ (Fig. 14a). The slope $s^q(t)$ (Fig. 15a) ranges between 1.0 and 1.4 during the integration time, except near $t = 16\ t_{ip}$ when there is a minimum of the average vertical velocity $\langle |w| \rangle$ (Fig. 15c). As expected, the larger the maximum PV anomaly of the flow, that is, the larger the Rossby number, the larger the deviation of the slope $s^q(t)$ from 1. The probable uncertainty $\sigma^q(t)$ (Fig. 15b) is greatest when $\langle |w| \rangle$ is smallest. The extreme values of $\langle |w| \rangle$ occur during vortex formation and subsequent merging. These events

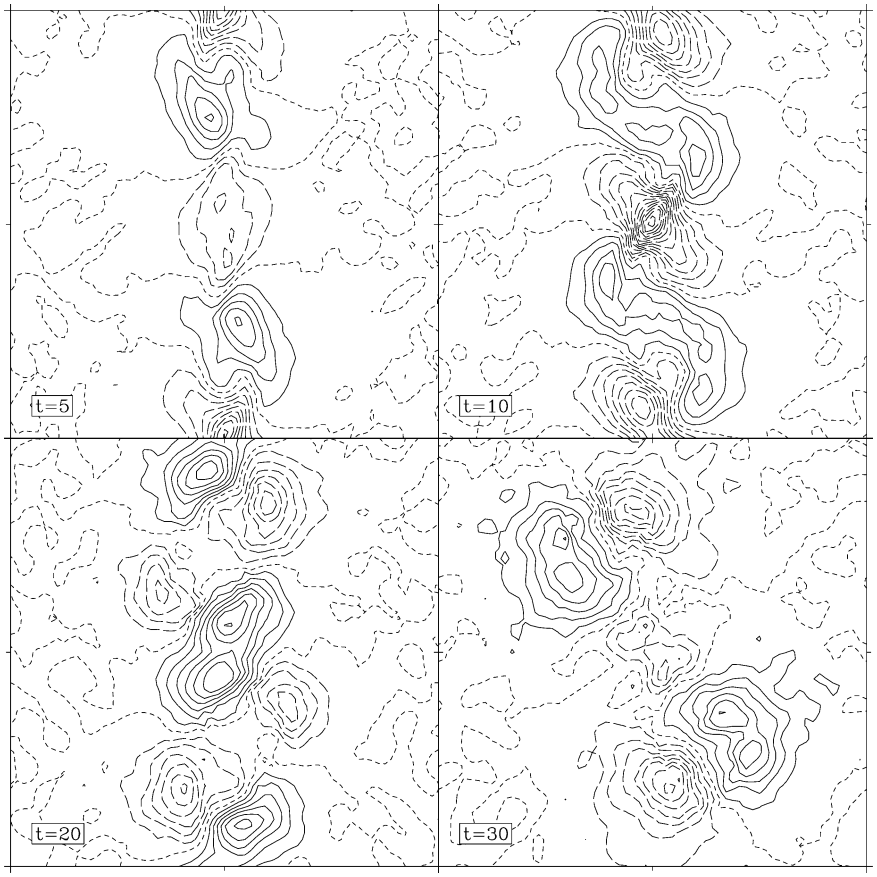

FIG. 12. Vertical velocity w (as in Fig. 2) for the case $\varpi_0 = 1.25$. Contour interval Δ is 1×10^{-5}.

occur faster the larger the PV anomaly, as can be observed in Figs. 15b and 15c. The scatter for positive vorticity flows is always larger than for negative PV flows (cf. Figs. 5b and 15b).

As for negative PV flows, the main reason why w^q differs from w in positive PV flows may be traced back to the omission of the term $\tilde{\boldsymbol{\zeta}}'_h \cdot \nabla_h^2 \mathbf{u}_h$. Adding this term to the right-hand side of (6) results in a decrease of the slope in the scatterplots in Fig. 14b. In this case the ageostrophic horizontal pseudovorticity $\tilde{\boldsymbol{\zeta}}'_h$ (Fig. 16a) is always directed into the anticyclonic vortices, meaning that the ageostrophic shear velocity $\mathbf{u}'_z$ is mainly in the same direction as $\mathbf{u}_h$; that is, the vortices are again supergeostrophic. The Laplacian $\nabla_h^2 \mathbf{u}_h$ (Fig. 16b) is mainly opposite to $\mathbf{u}_h$. The product of both terms $\tilde{\boldsymbol{\zeta}}'_h \cdot \nabla_h^2 \mathbf{u}_h$ (Fig. 16c) becomes negative (positive) upstream (downstream) of the troughs, that is, of the opposite sign to the divergence of $\mathbf{Q}_h^q$ (Fig. 16d), which is always larger in magnitude. Thus, $\tilde{\boldsymbol{\zeta}}'_h \cdot \nabla_h^2 \mathbf{u}_h$ is a term that decreases the magnitude of the vertical velocity in the generalized ω equation. It is expected therefore that the omission of this term in the QG ω equation will generally result in the overestimation of the vertical velocity in flows with positive PV.

The second most important term in (7), missing in (6), is again $2\nabla_h \cdot Q'_h$. Including this term in (6) results also in an improvement in the slope (Fig. 14c). Taking into account the rate of change of the ageostrophic differential vertical vorticity, $\tilde{\zeta}'_{zt} + \mathbf{u}_h \cdot \boldsymbol{\nabla}_h \tilde{\zeta}'_z$ (Fig. 14d) again reduces the scatter.

The SG vertical velocity w^s (Fig. 17) reproduces the quadrupole pattern of w as well, is free of inertia–gravity waves, and its magnitude is now significantly smaller than that of w^q. The scatterplot of w^s versus w at $t = 20\ t_{\text{ip}}$ (Fig. 14e) shows a slope close to 1, as confirmed by the values of $s^s(t)$ during the time evolution and for the different values of ϖ_0. The scatter of w^s (Fig. 14e) does not, however, seem to be smaller than that of w^q (Fig. 14a), as confirmed by the values of $\sigma^s(t)$ (Fig. 15b). Thus, the SG solution, though having a scatter comparable to that of the QG solution, improves the slope in the linear regression, and thus is better able to approximate the larger vertical velocities. (Note that the statistical values in Fig. 15 are computed using magnitudes of w larger than 0.5×10^{-5}.)

The scatter in cases with positive PV anomalies may again be related to the presence of inertia–gravity waves. The average spectra of the squared vertical velocity w^2

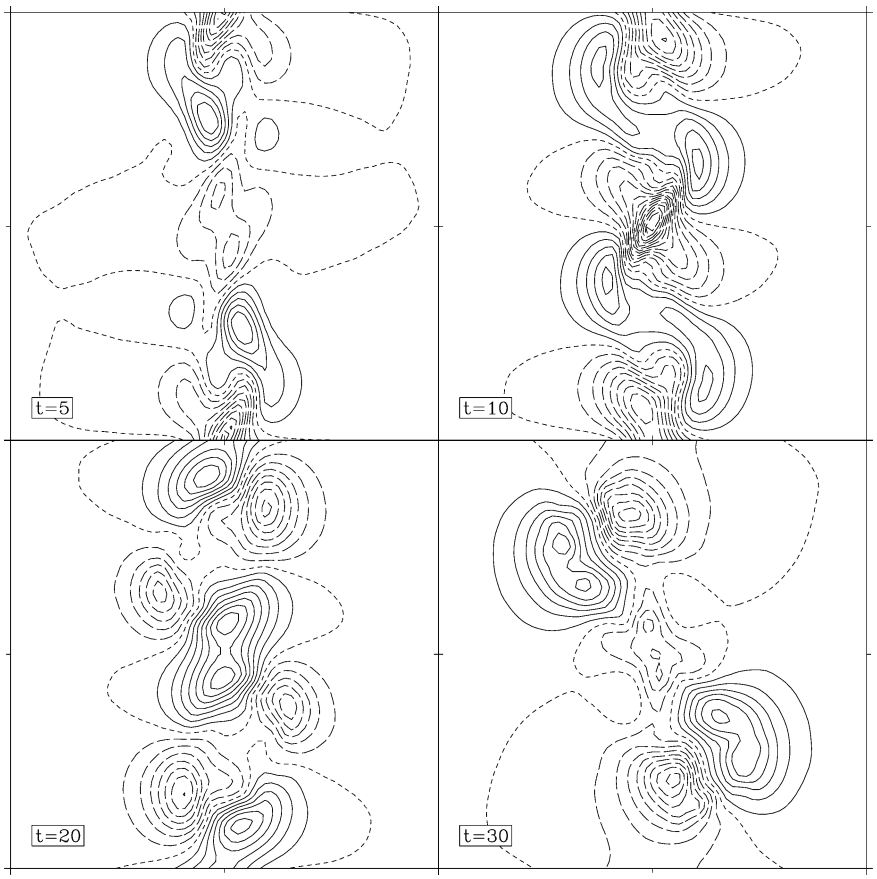

FIG. 13. As in Fig. 12 but for the QG vertical velocity w^q.

(Fig. 18a) show inertia–gravity wave motion, though this time weaker than that present in the negative PV anomaly cases (Fig. 8a). The presence of inertia–gravity waves is a consequence of the reduced diffusivity of the model, which is small enough to avoid a serious damping of the motion at these frequencies. Despite the inertia–gravity waves, the vertical motion is still close to a balanced state since the spectral components of w^2 at low frequencies dominate (Fig. 18a). The magnitude of w^2 and the kinetic energy increases with the PV anomaly at all frequencies (Fig. 18b).

These gravity waves appear to arise from spontaneous generation during the evolution of the flow, and not from the imbalance in the initial conditions. A spectrogram (Fig. 19) shows that the gravity wave components reach maximum values at about $t = 13t_{ip}$ and $t = 23\ t_{ip}$, that is, later than the end of the initialization period ($t = 5t_{ip}$). The first episode seems to happen when the PV cylinder breaks into two vortices. The second episode is perhaps related to the collision of the two vortices.

c. Jet current

As an example of an oceanic feature displaying both positive and negative PV anomalies a jet current is simulated with two horizontal PV cylinders of opposite sign (Fig. 20). This configuration induces a strong northward jet with two smaller southward currents running along the flanks of the two-cylinder system. Each cylinder has a horizontal dimension of $0.5c$ as before, but a larger vertical dimension of $1/\sqrt{2}$ so that the two cylinders touch each other at the origin and just fit within a circle of radius $0.5c$ (after stretching the height coordinate by c). We take the maximum and minimum PV anomalies to be $\varpi_0 = \pm 0.75$. The time average of the (minimum) Rossby number is -0.67 and the time average of the maximum Froude number is 0.39. As the flow evolves, the PV rolls up into a street of large cyclonic and anticyclonic vortices that couple, forming the familiar mushroomlike eddy structures, from which small-scale eddies are afterward detached. Large vertical velocities (Fig. 21a) are associated with the most compact mushroomlike vortex, located in the northern part of the domain at $t = 20t_{ip}$. This field exhibits the characteristic quadrupole patterns seen before, but the amplitudes are here significatively larger (cf. with Figs. 2 and 12). Mushroomlike eddies therefore enhance vertical motion.

Both the QG and SG solutions (Figs. 21b,c) reproduce the quadrupole pattern of w and filter the inertia–gravity

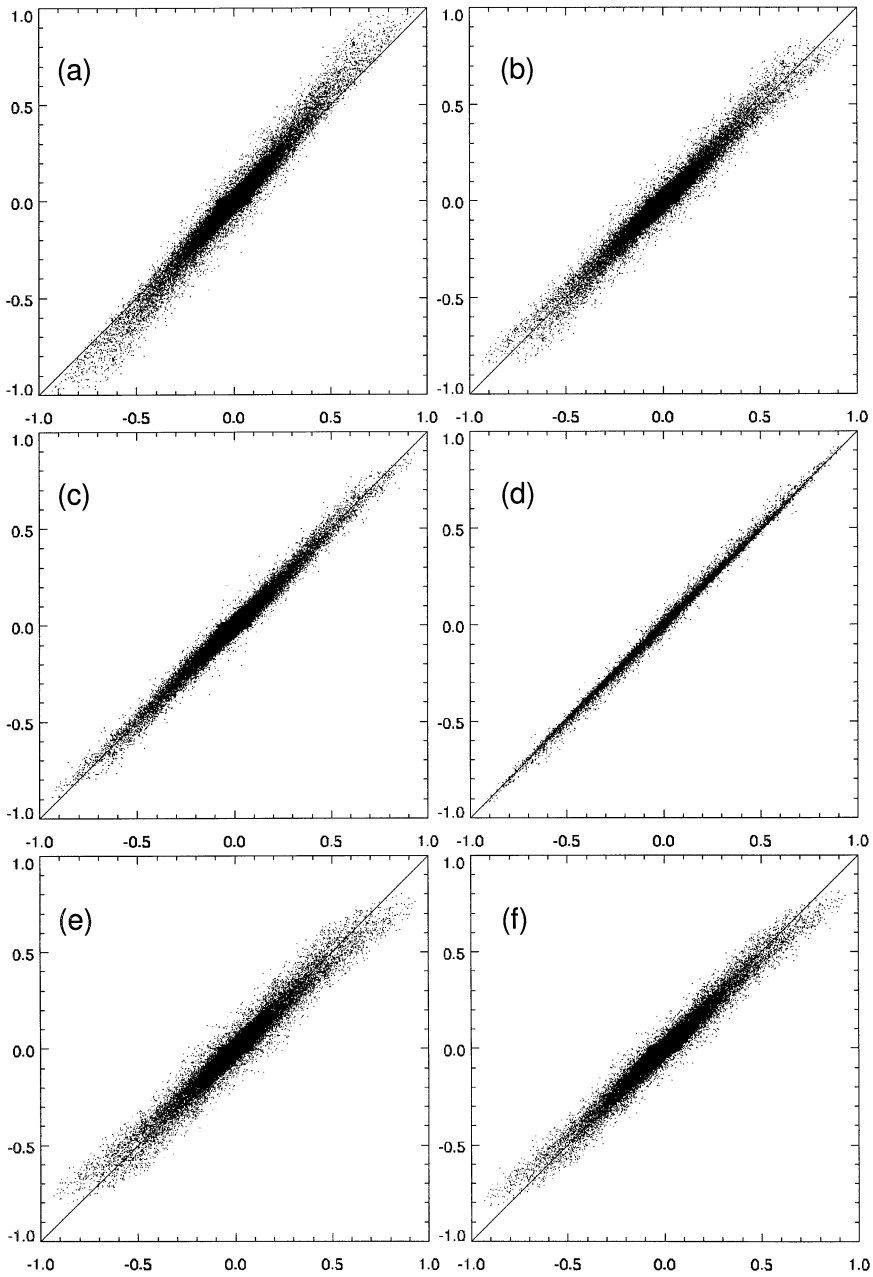

FIG. 14. Scatterplots, as in Fig. 4, for the case $\varpi_0 = 1.25$ and $e_f = 10$.

waves. The important difference with respect to the previous cases is that the SG solution does not seem to improve the QG one. The scatter of the w^s solution (Fig. 22e) is clearly broader, for large vertical velocities, than that of w^q (Fig. 22a). The difference fields $w - w^q$ and $w - w^s$ (Figs. 21d,e) show both larger differences where the vertical velocity changes sign (where the horizontal gradient of w is larger), which is due to a spatial offset of the extreme values of both w^q and w^s with respect to w. This offset might be related to the large local change of PV caused by the fast propagation of the mushroomlike eddy. These fields show that w^q is, in this case, a better approximation to w than is w^s. This fact is true for almost the entire simulation as can be seen from the time series of the domain average values of $w - w^q$ and $w - w^s$ (Fig. 23).

Apparently, the reason for this anomalous behavior of w^s is due not to the usual SG approximations, but to an additional approximation of volume conservation normally adopted to derive the ω^s equation (see appendix B). This assumption affects w^s partly because it neglects the term

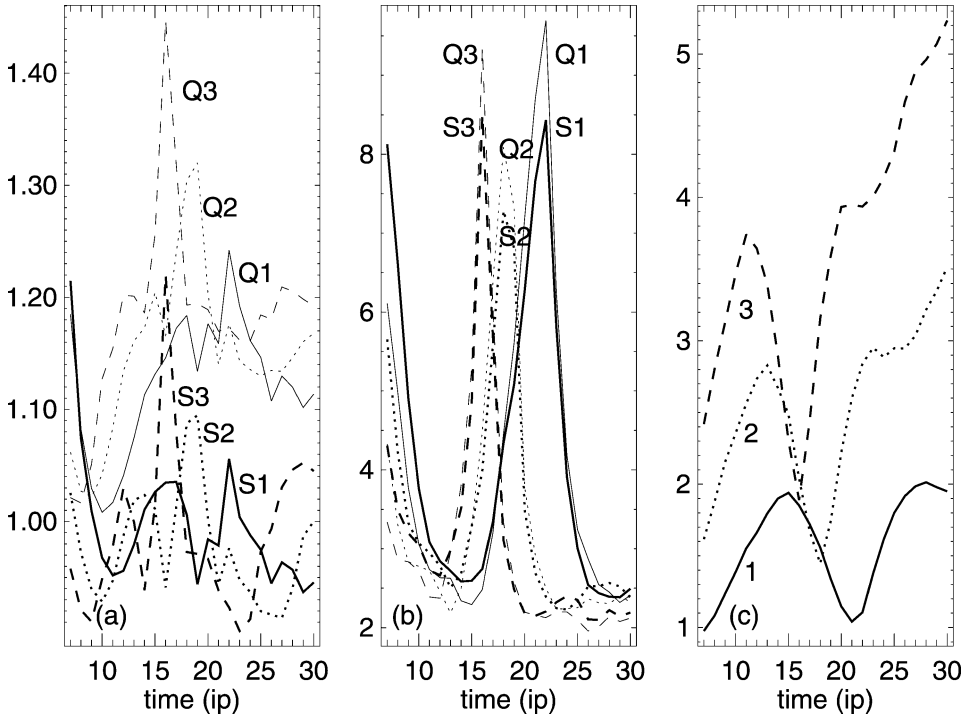

FIG. 15. As in Fig. 5 but for the case $e_f = 10$ and $\varpi_0 = 0.75$ (label 1), $\varpi_0 = 1.00$ (label 2), and $\varpi_0 = 1.25$ (label 3).

$$-\frac{\partial J'}{\partial \hat{z}},$$

where

$$J' \equiv \frac{1}{\zeta^s}(J_{xy}\{u^g, u'\} + J_{xy}\{v^g, v'\}),$$

on the right-hand side of the ω^s equation [(2)]. Including this term in (2) results in an improvement of the scatter (Fig. 22f). This improvement also occurs in the cases having only negative or only positive PV anomalies (Figs. 4f and 22f). However, it is only in the jet case that this term makes the SG solution w^s better than the QG solution w^q (Fig. 23).

There is also another important difference, with respect to the previous cases, concerning the QG solution. In the present jet case the main reason for the deviation of w^q from w is not the absence of the term $\tilde{\boldsymbol{\zeta}}'_h \cdot \nabla_h^2 \mathbf{u}_h$. Adding *only* this term to the right hand side of (6) does not result in a reduction of the scatter (Fig. 22b). The term $2\boldsymbol{\nabla}_h \cdot \mathbf{Q}'_h$ in (6) is also needed to improve the slope and reduce the scatter (Fig. 22c) as well as the rate of change of the ageostrophic differential vertical vorticity $\tilde{\zeta}'_{zt} + \mathbf{u}_h \cdot \boldsymbol{\nabla}_h \tilde{\zeta}'_z$ (Fig. 22d). The final scatter (Fig. 22d) is still larger than those for only negative PV flows (Fig. 4d) or positive PV flows (Fig. 14d) because a new term also becomes important in the generalized ω equation. This new term is $\tilde{\zeta} w^q_{zz}$. Taking into account only this term in the QG ω equation [(6)], solved using a relaxation method, reduces significatively the scatter of w^q (Fig. 24a, with $\langle |w - w^q| \rangle / \langle |w| \rangle = 0.41$), which is clearly a better approximation to w than is w^s (Fig. 22e, with $\langle |w - w^s| \rangle / \langle |w| \rangle = 0.44$). Using, instead, the geostrophic part $\tilde{\zeta}^g w^q_{zz}$ does not significatively change the result in Fig. 24a so that either $\tilde{\zeta}^g w^q_{zz}$ or $\tilde{\zeta} w^q_{zz}$ can be used. Taking into account $\tilde{\zeta} w^q_{zz}$ as well as the other important terms previously identified ($\tilde{\boldsymbol{\zeta}}'_h \cdot \nabla_h^2 \mathbf{u}_h$, $2\boldsymbol{\nabla}_h \cdot \mathbf{Q}'_h$, and $\tilde{\zeta}'_{zt} + \mathbf{u}_h \cdot \boldsymbol{\nabla}_h \tilde{\zeta}'_z$), remarkably precise vertical velocities are obtained (Fig. 24b).

4. Conclusions

The vertical velocity from a number of high-resolution numerical simulations using an explicitly PV-conserving three-dimensional numerical model has been analyzed and compared with the solutions of the QG and SG ω equations. The SG solution has been derived in a novel way in physical coordinates. The results obtained clarify the roles played by PV, diffusion, and inertia–gravity wave motion as regards the accuracy of the QG and SG vertical velocity estimates. For negative PV flows, the magnitudes of w^q and w^s are smaller than the magnitude of w, while they are larger for positive PV flows. It was found that the main reason for the deviation of w^q from w is the neglect of the term $\tilde{\boldsymbol{\zeta}}'_h \cdot \nabla_h^2 \mathbf{u}_h$ in the QG ω equation. The other important terms are $2\boldsymbol{\nabla}_h \cdot \mathbf{Q}'_h$ and the rate of change of ageostrophic differential vorticity.

The SG solution w^s is always more accurate than the QG solution w^q for large vertical velocity values and

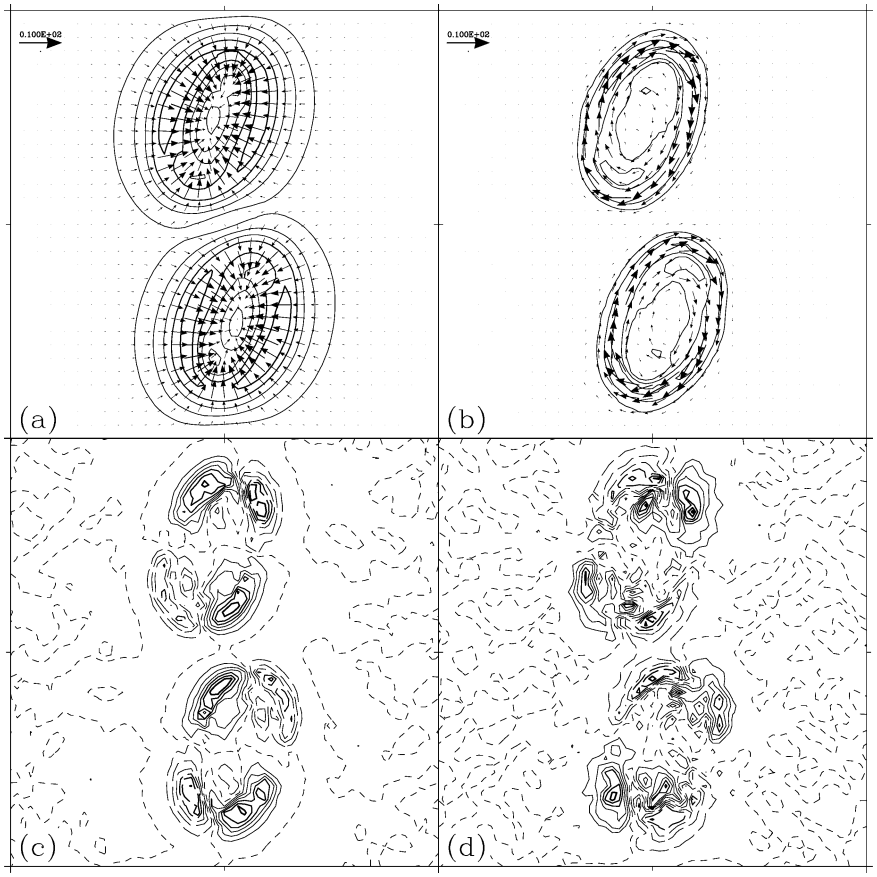

FIG. 16. As in Fig. 6 but for the case with $\varpi_0 = 1.25$. (a) Ageostrophic horizontal pseudovorticity $\tilde{\boldsymbol{\zeta}}_h'$ ($\Delta = 2.5$, reference vector is 25), (b) horizontal Laplacian of the horizontal velocity $\nabla_h^2\mathbf{u}_h$ ($\Delta = 10^{-4}$, reference vector is 5×10^{-4}), (c) $\tilde{\boldsymbol{\zeta}}_h' \cdot \nabla_h^2\mathbf{u}_h$ ($\Delta = 0.25 \times 10^{-4}$), and (d) $2\nabla_h \cdot \mathbf{Q}^g$ ($\Delta = 0.25 \times 10^{-3}$).

when the flow contains only PV anomalies of one sign. However, the scatter in w versus w^q and w versus w^s, arising from the spontaneous generation of inertia–gravity waves, is similar. These waves may be damped using higher diffusion but then the amount of diffusion can become more important in the absolute comparison of vertical velocity than the choice of the QG or SG approximation. In other words, diffusion makes the assessment of these approximations difficult.

For flows with both positive and negative PV anomalies, for example mushroomlike eddies, a new term ($\tilde{\zeta}w_{zz}$) becomes important in the ω equation. In these flows w^q is, in fact, a better approximation to w than is w^s. This surprising result appears to be due to an additional assumption related to volume conservation in geostrophic coordinates, normally adopted in deriving the SG ω equation.

A complete analysis of the SG ω equation to validate the importance of the missing terms requires an analysis, term by term, of a generalized ω equation, that is, an ω equation similar to the SG ω equation but consistent with the exact balance of momentum and mass conservation. However, none of the generalized ω equations derived by Krishnamurti (1968), Davies-Jones (1991), or Viúdez et al. (1996b), though clear generalizations of some form of the QG ω equation, seem to be a generalization of the SG ω equation. A derivation of such an equation would be immensely useful.

If both density and horizontal velocity are known, the terms $-\tilde{\boldsymbol{\zeta}}_h' \cdot \nabla_h^2\mathbf{u}_h$, the total part of the divergence of the Q vector $-\boldsymbol{\nabla}_h \cdot (\boldsymbol{\nabla}_h\mathbf{u}_h \cdot \boldsymbol{\nabla}_h D)$, and the absolute vertical vorticity $\zeta + f$ can be combined into an improved ω equation

$$c^2\nabla_h^2 w + (\tilde{\zeta} + 1)w_{zz} = 2\boldsymbol{\nabla}_h\mathbf{u}_h : \boldsymbol{\nabla}_h\boldsymbol{\nabla}_h D + (\tilde{\boldsymbol{\zeta}}_h + \boldsymbol{\nabla}_h D) \cdot \nabla_h^2\mathbf{u}_h. \quad (8)$$

For experimental purposes, when both experimental density and horizontal current data are available, but the accuracy of the latter is not sufficient to obtain w_z from volume conservation ($\boldsymbol{\nabla} \cdot \mathbf{u} = 0$), the above equation is recommended for estimating the mesoscale vertical velocity. This is usually the case with data obtained from ship-mounted acoustic Doppler current-meter profiles.

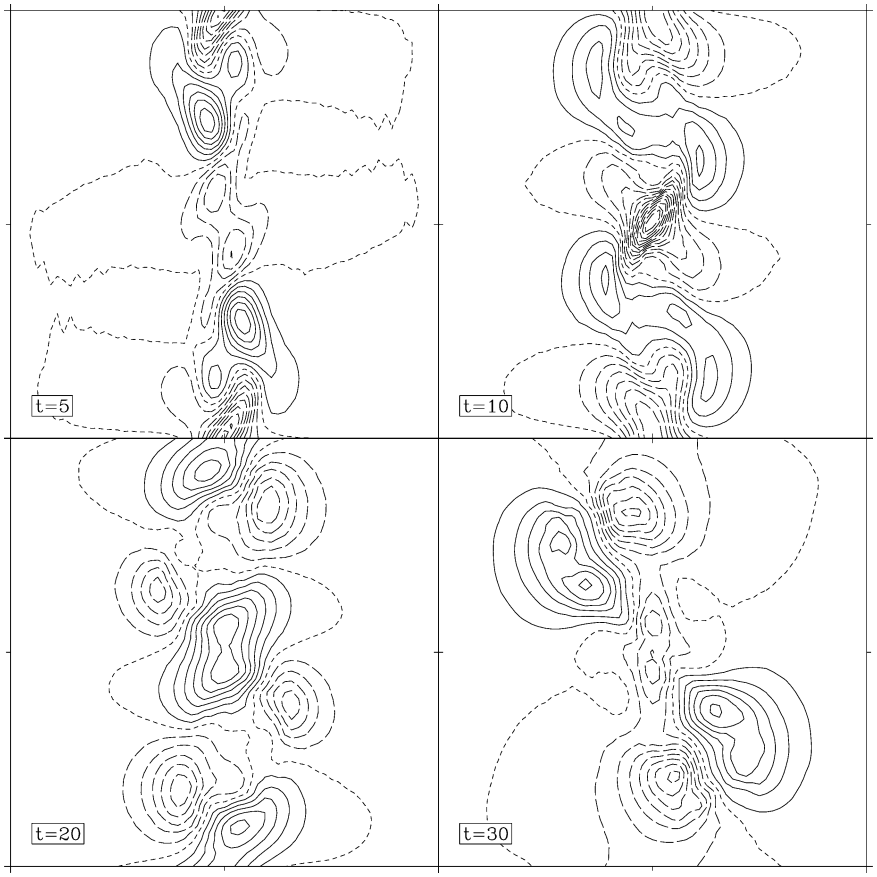

FIG. 17. As in Fig. 12 but for the SG vertical velocity w^s.

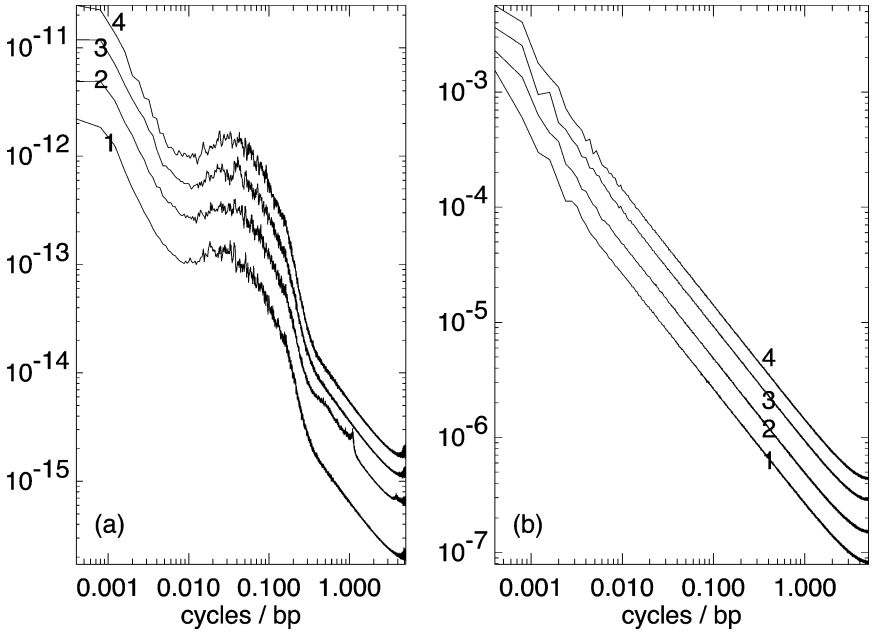

FIG. 18. As in Fig. 8 but for $e_f = 10$ and $\varpi_0 = 0.75$ (label 1), $\varpi_0 = 1.00$ (label 2), $\varpi_0 = 1.25$ (label 3), and $\varpi_0 = 1.50$ (label 4).

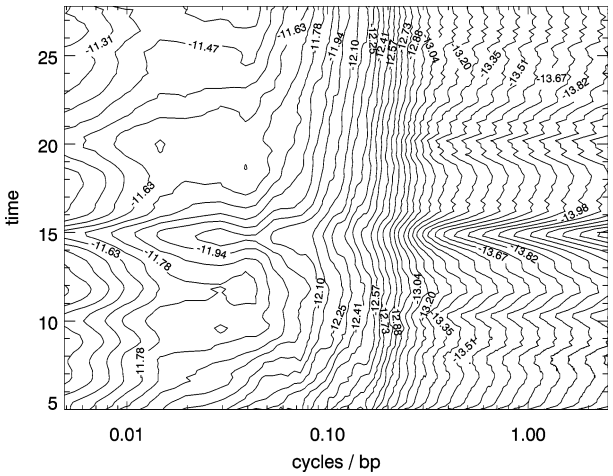

FIG. 19. Average spectrogram (or average ''running spectra'') of w^2 for the case $\varpi = 1.25$ and $e_f = 10$. Every spectral window has 2048 data points (about two inertial periods). The x axis is the period in cycles per buoyancy period, and the y axis is the central time, in inertial periods, of the spectral window. The spectrogram jump is 200 data points (0.2 inertial periods) so that the spectrogram distribution involves number of frequencies $\times$ number of spectra = 1025 $\times$ 116 data points. This spectrogram is the average of 8^3 spectrograms corresponding to 8^3 time series equally distributed in the domain. The x axis and the data are in logarithmic scale.

Equation (8) is in direct-vector (coordinate independent) notation. Its expression in Cartesian components and in terms of the density field is given in appendix C.

Acknowledgments. Support for this research has come from the Spanish Ministerio de Ciencia y Tecnología Grant REN2002-01343 and the program Ramón y Cajal 2001, as well as the UK National Environmental Research Council (Grant GR3/11899).

APPENDIX A

The Prognostic Variables Used in the Numerical Models

For volume-preserving flows the three-dimensional velocity potential $\boldsymbol{\varphi} \equiv (\varphi, \psi, \phi)$ defines the velocity $\mathbf{u}$ and the scaled isopycnal displacement D as follows:

$$\mathbf{u} = -\boldsymbol{\nabla} \times \boldsymbol{\varphi}, \qquad D = -\boldsymbol{\nabla} \cdot \boldsymbol{\varphi}.$$

Let $\mathcal{A}^* \equiv (\mathcal{A}, \mathcal{B}, \mathcal{C}) \equiv \tilde{\boldsymbol{\omega}} - \boldsymbol{\nabla} D = \nabla^2 \boldsymbol{\varphi} = (\nabla^2 \varphi, \nabla^2 \psi, \nabla^2 \phi)$, where $\tilde{\boldsymbol{\omega}}$ is the dimensionless vorticity. The vector $\mathcal{A}_h^*$ is the dimensionless ageostrophic horizontal vorticity.

The $\mathcal{AB}\varpi$ model employs $\mathcal{A}$, $\mathcal{B}$, and the PV anomaly

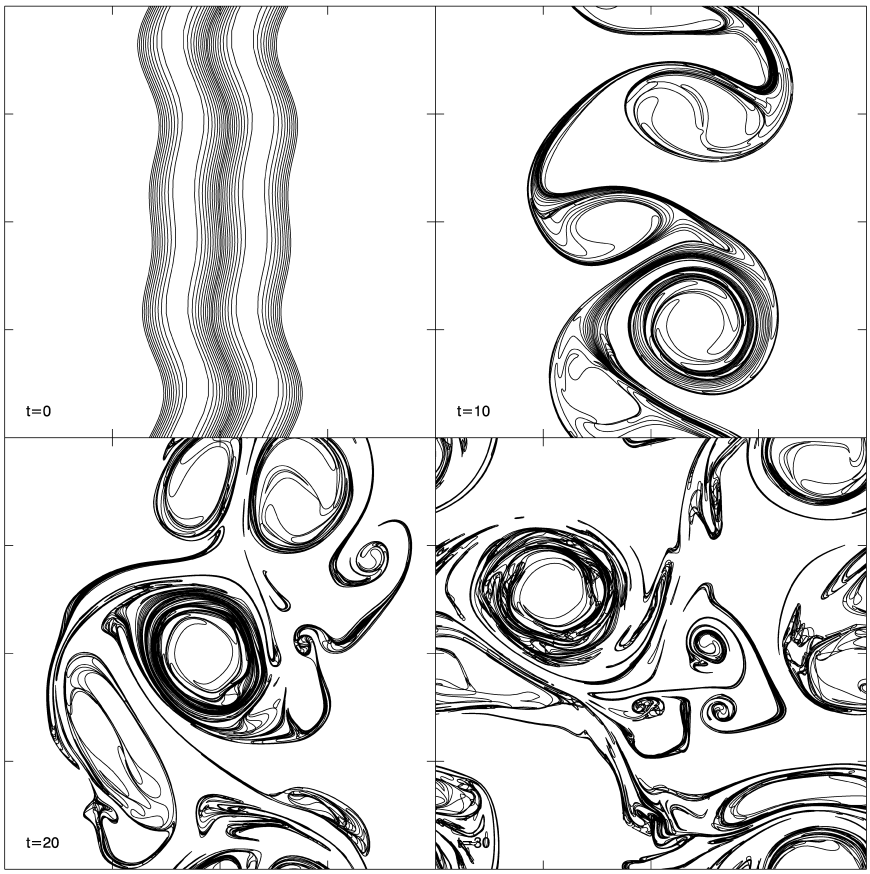

FIG. 20. Time evolution (as in Fig. 1) of the PV contours for the jet current with max/min PV anomalies $\varpi_0 = \pm 0.75$ and $e_f = 10$.

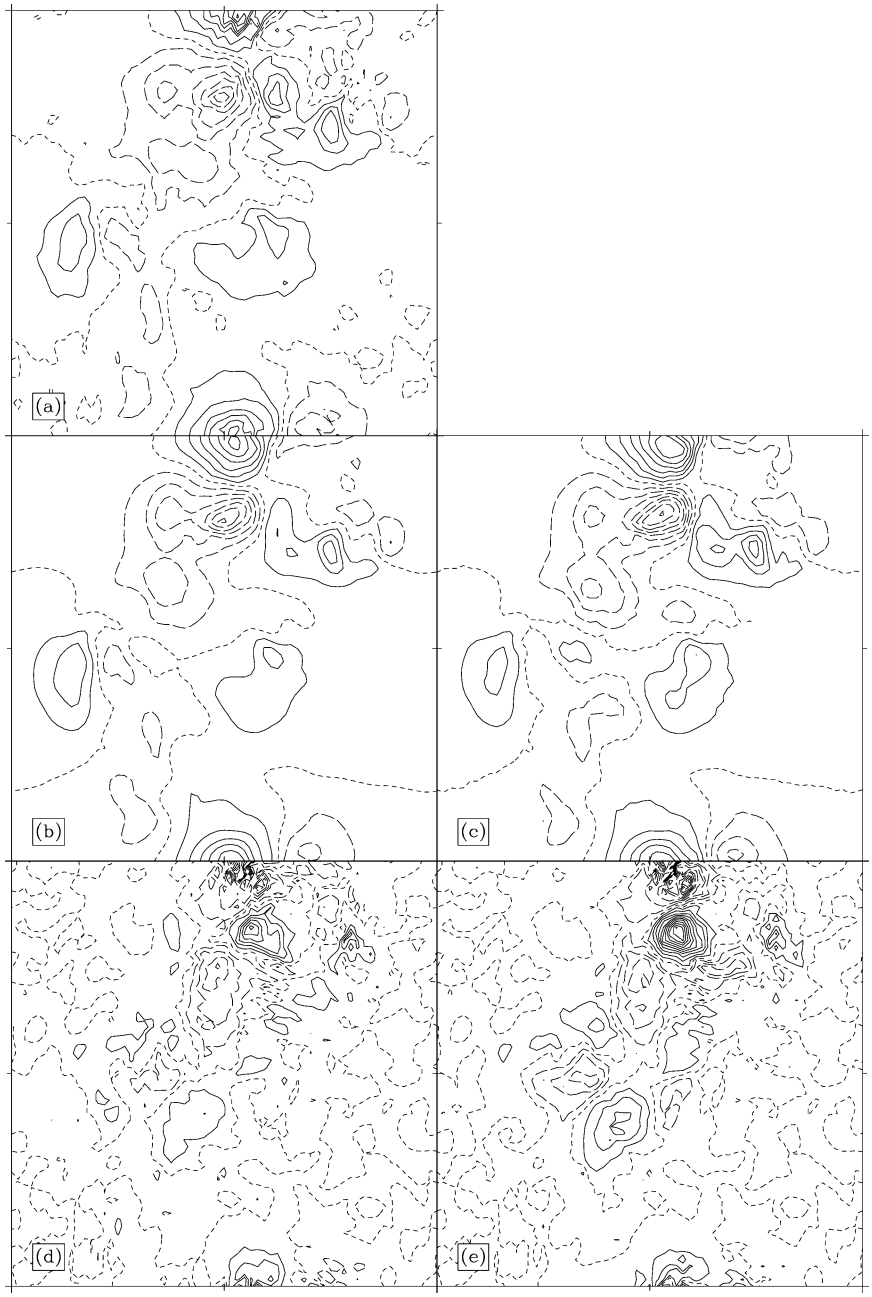

FIG. 21. Horizontal distributions of (a) w ($\Delta = 5 \times 10^{-5}$), (b) w^q ($\Delta = 5 \times 10^{-5}$), (c) w^s ($\Delta = 5 \times 10^{-5}$), (d) $w - w^q$ ($\Delta = 2.5 \times 10^{-5}$), and (e) $w - w^s$ ($\Delta = 2.5 \times 10^{-5}$), for the jet current at $t = 20\ t_{ip}$ and horizontal layer $l_z = 28$.

ϖ as prognostic variables. After each time step, the horizontal potential vector $\boldsymbol{\varphi}_h$ is obtained from $\boldsymbol{\varphi}_h = \nabla^{-2}\mathcal{A}_h^*$, while ϕ is obtained from the inversion of the definition of ϖ. The dimensionless PV density is defined by

$$\Pi \equiv \tilde{\boldsymbol{\omega}}^q \cdot \nabla d = (\tilde{\boldsymbol{\omega}} + \mathbf{k}) \cdot (\mathbf{k} - \epsilon^2 \nabla D)$$
$$= 1 + \tilde{\zeta} - \epsilon^2 D_z - \epsilon^2 \tilde{\boldsymbol{\omega}} \cdot \nabla D.$$

Since $\tilde{\zeta} = \nabla_h^2 \phi - \nabla_h \cdot \boldsymbol{\varphi}_{hz}$, and replacing $\tilde{\boldsymbol{\omega}} = \mathcal{A}^* + \nabla D$, the dimensionless PV anomaly $\varpi \equiv \Pi - 1$ may be written in terms of $\boldsymbol{\varphi}$ as

$$\varpi = \mathcal{L}^q\{\phi\} - (1 - \epsilon^2)\nabla_h \cdot \boldsymbol{\varphi}_{hz}$$
$$+ \epsilon^2[\nabla^2 \boldsymbol{\varphi} - \nabla(\nabla \cdot \boldsymbol{\varphi})] \cdot \nabla(\nabla \cdot \boldsymbol{\varphi}),$$

where the linear operator $\mathcal{L}^q \equiv \nabla_h^2 + \epsilon^2 \partial_{zz}$ is the QG

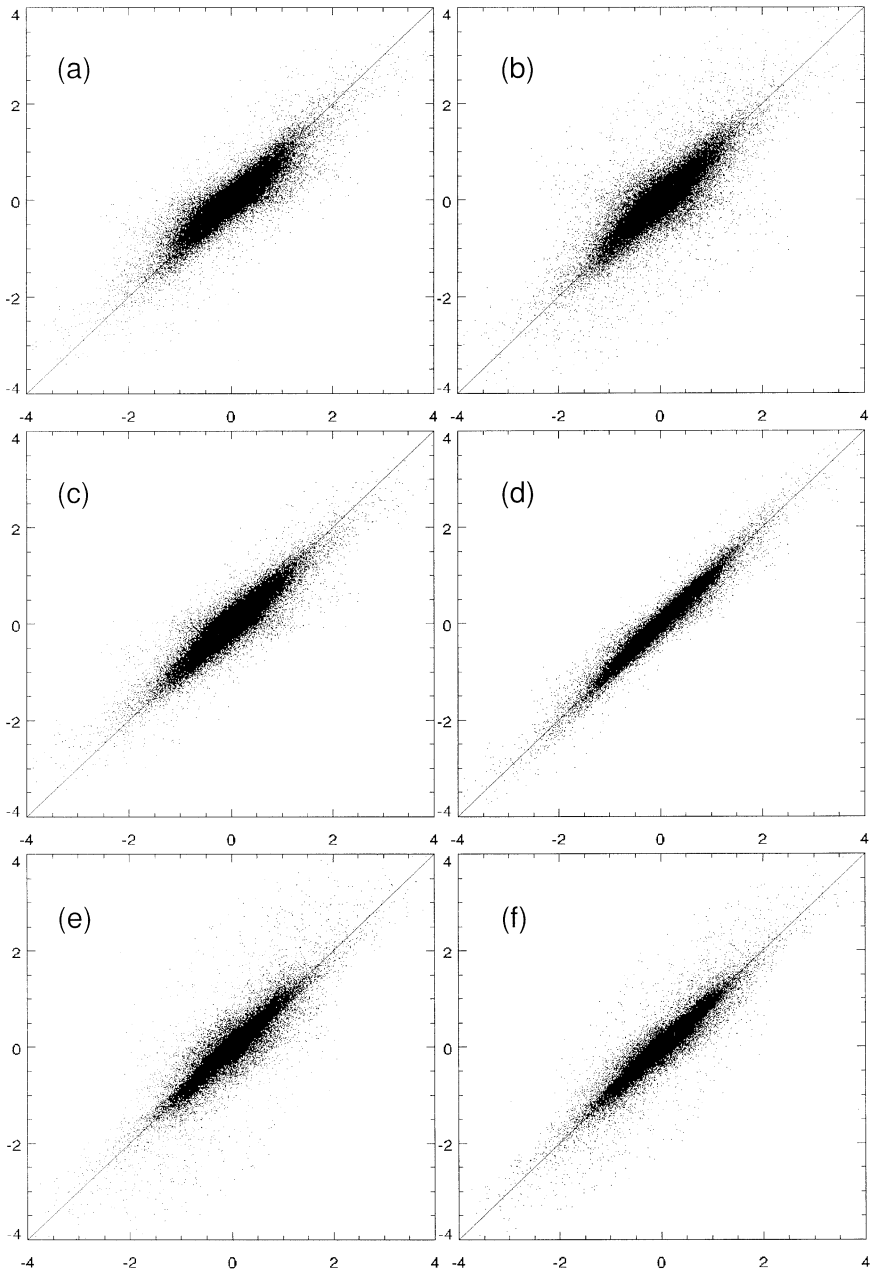

FIG. 22. Scatterplots, as in Fig. 4, for the jet current case with $\varpi_0 = \pm 0.75$ and $e_f = 10$.

Laplacian operator. The $\mathcal{AB}\varpi$ model inverts the above expression to obtain ϕ from φ, ψ, and ϖ.

The $\mathcal{ABC}$ model employs instead the three components of $\mathcal{A}^*$ as prognostic variables. After each time step, the vector potential is obtained from the inversion $\boldsymbol{\varphi} = \nabla^{-2}\mathcal{A}^*$. In this procedure there is no need to invert the PV definition, but it has the disadvantage that PV is not explicitly conserved. As a result, substantially more diffusion is required to obtain numerically stable solutions than in the $\mathcal{AB}\varpi$ model.

APPENDIX B

The SG Volume Conservation Approximation

The SG dynamical approximation replaces the advection of total velocity with the advection of geostrophic velocity in the horizontal momentum equation. In the derivation of the SG ω equation, it is further assumed that

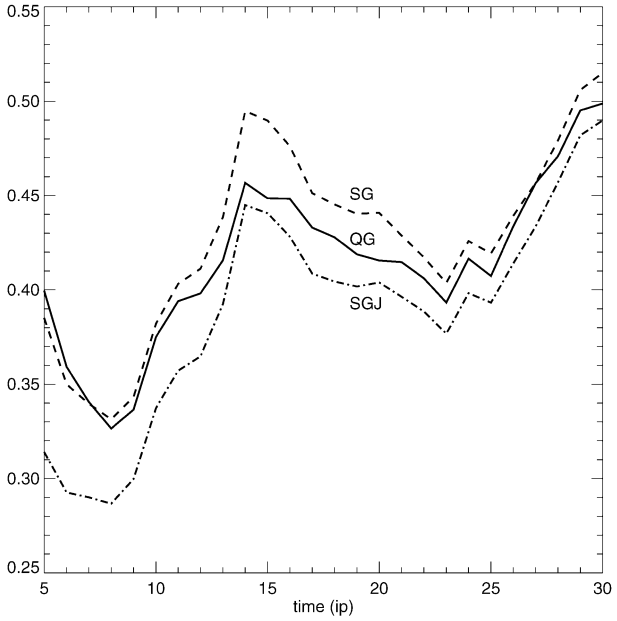

FIG. 23. Time series, for the jet current case with $\varpi_0 = \pm 0.75$ and $e_f = 10$, of the relative spatial averages $\langle |w - w^q| \rangle / \langle |w| \rangle$ (symbol QG), $\langle |w - w^s| \rangle / \langle |w| \rangle$ (symbol SG), and $\langle |w - w^{sJ}| \rangle / \langle |w| \rangle$ (SGJ, where w^{sJ} is obtained by solving the SG ω equation including the term $-J'_{\hat{z}}$).

$$\hat{u}^{ag}_{\hat{x}} + \hat{v}^{ag}_{\hat{y}} + \hat{w}_{\hat{z}} \approx 0 \tag{B1}$$

(Hoskins and Draghici 1977), where

$$\hat{u}^{ag} \equiv u - u^g + w\tilde{v}^g_{\hat{z}} \quad \text{and} \quad \hat{v}^{ag} \equiv v - v^g - w\tilde{u}^g_{\hat{z}}.$$

In the space $(\mathbf{x}, t)$,

$$\hat{u}^{ag}_{\hat{x}} + \hat{v}^{ag}_{\hat{y}} + \hat{w}_{\hat{z}} = \frac{f}{\zeta^s}(u'_x + v'_y + w_z) + \underbrace{\frac{1}{\zeta^s}(J_{xy}\{u^g, u'\} + J_{xy}\{v^g, v'\})}_{J'} + \frac{1}{\zeta^s}(\mathcal{F}\{w, \nabla w\}),$$

where $(u', v') \equiv (u, v) - (u^g, v^g)$ is the ageostrophic horizontal velocity, and $\mathcal{F}\{w, \nabla w\}$ is a function of w and its gradient. Since $u'_x + v'_y + w_z = 0$ exactly, the approximation (B1) assumes that the term J' is small as compared with $\hat{w}_{\hat{z}}$ or, equivalently with $\hat{u}^{ag}_{\hat{x}} + \hat{v}^{ag}_{\hat{y}}$. We found that, in a time and space average sense, J' was always smaller but of the same order of magnitude as $\hat{w}_{\hat{z}}$. For instance, in the oceanic jet with $\varpi_0 = \pm 0.75$ and at $t = 20\ t_{\text{ip}}$, the ratio of the mean values of these terms was found to be $\langle |J'| \rangle / \langle |\hat{w}_{\hat{z}}| \rangle = 0.36$.

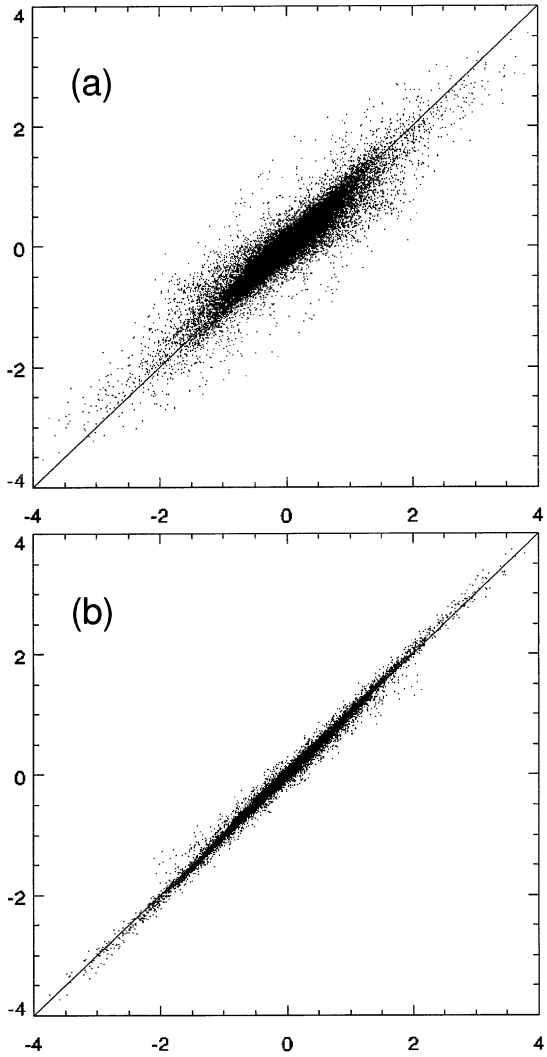

FIG. 24. Scatterplots of the total velocity w (horizontal axis, in units of 10^{-4}), for the jet current case with $\varpi_0 = \pm 0.75$ and $e_f = 10$, vs (vertical axis) (a) the vertical velocity that results from including $\tilde{\zeta} w_{zz}$ on the left-hand side of the w^q equation (6) and (b) the vertical velocity that results from including $\tilde{\zeta} w_{zz}$ and $\tilde{\boldsymbol{\zeta}}'_h \cdot \nabla^2_h \mathbf{u}_h + 2\nabla_h \cdot \mathbf{Q}'_h + \tilde{\zeta}'_{zt} + \mathbf{u}_h \cdot \nabla_h \tilde{\zeta}'_z$ in (6). Data for the entire domain are shown at $t = 20\ t_{\text{ip}}$.

APPENDIX C

Equation (8) in Cartesian Components

In Cartesian components, (8) is

$$N^2(w_{xx} + w_{yy}) + f^2\left(\frac{v_x - u_y}{f} + 1\right)w_{zz} = 2[u_x \varrho_{xx} + v_y \varrho_{yy} + (u_y + v_x)\varrho_{xy}] + (-fv_z + \varrho_x)(u_{xx} + u_{yy}) + (fu_z + \varrho_y)(v_{xx} + v_{yy}),$$

where $N^2 \equiv -g\overline{\rho_z}/\rho_0$ and $\varrho \equiv g\rho/\rho_0$.

REFERENCES

Allen, J. T., and D. A. Smeed, 1996: Potential vorticity and vertical velocity at the Iceland–Færoes front. *J. Phys. Oceanogr.,* **26,** 2611–2634.

Davies-Jones, R., 1991: The frontogenetical forcing of secondary circulations. Part I: The duality and generalization of the *Q* vector. *J. Atmos. Sci.,* **48,** 497–509.

Dritschel, D. G., and M. H. P. Ambaum, 1997: A contour-advective semi-Lagrangian algorithm for the simulation of fine-scale conservative fields. *Quart. J. Roy. Meteor. Soc.,* **123,** 1097–1130.

——, and A. Viúdez, 2003: A balanced approach to modeling rotating stably-stratified geophysical flows. *J. Fluid Mech.,* **488,** 123–150.

Eliassen, A., 1949: The quasi-static equations of motion with pressure as independent variable. *Geophys. Publ.,* **17**(3), 1–44.

Fiekas, V., H. Leach, K.-J. Mirbach, and J. D. Woods, 1994: Mesoscale instability and upwelling. Part I: Observations at the North Atlantic Intergyre Front. *J. Phys. Oceanogr.,* **24,** 1750–1758.

Holton, J. R., 1992: *An Introduction to Dynamic Meteorology.* 3d ed., Academic Press, 511 pp.

Hoskins, B. J., and I. Draghici, 1977: The forcing of ageostrophic motion according to the semigeostrophic equations and in an isentropic coordinate model. *J. Atmos. Sci.,* **34,** 1859–1867.

——, ——, and H. C. Davies, 1978: A new look at the ω-equation. *Quart. J. Roy. Meteor. Soc.,* **104,** 31–38.

Krishnamurti, T. N., 1968: A diagnostic balance model for studies of weather systems of low and high latitudes, Rossby number less than 1. *Mon. Wea. Rev.,* **96,** 197–207.

Leach, H., 1987: The diagnosis of synoptic-scale vertical motion in the seasonal thermocline. *Deep-Sea Res.,* **34,** 2005–2017.

Naveira Garabato, A. C., J. T. Allen, H. Leach, V. H. Strass, and R. T. Pollard, 2001: Mesoscale subduction at the Antarctic Polar Front driven by baroclinic instability. *J. Phys. Oceanogr.,* **31,** 2087–2107.

Panofsky, H. A., 1946: Methods of computing vertical motion in the atmosphere. *J. Meteor.,* **3,** 45–49.

Pinot, J.-M., J. Tintoré, and D.-P. Wang, 1996: A study of the omega equation for diagnosing vertical motions at ocean fronts. *J. Mar. Res.,* **54,** 239–259.

Pollard, R. T., and L. A. Regier, 1992: Vorticity and vertical circulation at an ocean front. *J. Phys. Oceanogr.,* **22,** 609–625.

Rudnick, D. L., 1996: Intensive surveys of the Azores front. 2. Inferring the geostrophic and vertical velocity fields. *J. Geophys. Res.,* **101,** 16 291–16 303.

Shearman, R. K., J. A. Barth, and P. M. Kosro, 1999: Diagnosis of the three-dimensional circulation associated with mesoscale motion in the California Current. *J. Phys. Oceanogr.,* **29,** 651–670.

——, ——, J. S. Allen, and R. L. Haney, 2000: Diagnosis of the three-dimensional circulation in mesoscale features with large Rossby number. *J. Phys. Oceanogr.,* **30,** 2687–2709.

Sherman, L., 1953: Estimates of the vertical velocity based on the vorticity equation. *J. Meteor.,* **10,** 399–400.

Strass, V. H., 1994: Mesoscale instability and upwelling. Part II: Testing the diagnostics of vertical motion with a three-dimensional ocean front model. *J. Phys. Oceanogr.,* **24,** 1759–1767.

Trenberth, K. E., 1978: On the interpretation of the diagnostic quasi-geostrophic omega equation. *Mon. Wea. Rev.,* **106,** 131–137.

Viúdez, A., and D. G. Dritschel, 2003: Vertical velocity in mesoscale geophysical flows. *J. Fluid Mech.,* **483,** 199–223.

——, J. Tintoré, and R. L. Haney, 1996a: About the nature of the generalized omega equation. *J. Atmos. Sci.,* **53,** 787–795.

——, ——, and ——, 1996b: Circulation in the Alboran Sea as determined by quasi-synoptic hydrographic observations. Part I: Three-dimensional structure of the two anticyclonic gyres. *J. Phys. Oceanogr.,* **26,** 684–705.

——, R. L. Haney, and J. T. Allen, 2000: A study of the balance of horizontal momentum in a vertical shearing current. *J. Phys. Oceanogr.,* **30,** 572–589.

Yudin, M. I., 1955: Invariant quantities in large-scale atmospheric processes. *Glav. Geofiz. Observ.,* **55,** 3–12.